

Production characteristics of light nuclei, hypertritons and Ω -hypernuclei in Pb+Pb collisions at

$$\sqrt{s_{NN}} = 5.02 \text{ TeV}^*$$

Rui-Qin Wang,^{1,†} Xin-Lei Hou,¹ Yan-Hao Li,¹ Jun Song,^{2,‡} and Feng-Lan Shao^{1,§}

¹*School of Physics and Physical Engineering, Qufu Normal University, Shandong 273165, China*

²*School of Physical Science and Intelligent Engineering, Jining University, Shandong 273155, China*

We extend an analytical nucleon coalescence model with hyperons to study productions of light nuclei, hypertritons, and Ω -hypernuclei in Pb+Pb collisions at $\sqrt{s_{NN}} = 5.02$ TeV. We derive the formula of the momentum distribution of two bodies coalescing into dibaryon states and that of three bodies coalescing into tribaryon states. We explain the available data of the coalescence factors B_2 and B_3 , the transverse momentum spectra, the averaged transverse momenta, the yield rapidity densities, yield ratios of the deuteron, antihelium-3, antitriton, hypertriton measured by the ALICE collaboration, and give predictions of different Ω -hypernuclei, e.g., $H(p\Omega^-)$, $H(n\Omega^-)$ and $H(pn\Omega^-)$. We particularly study the production correlations of different light (hyper-)nuclei and find two groups of interesting observables, the averaged transverse momentum ratios of light (hyper-)nuclei to protons (hyperons) and their corresponding yield ratios. The former group exhibits a reverse hierarchy of the nucleus size, and the latter is sensitive to the nucleus production mechanism as well as the nucleus's own size.

Keywords: Light nuclei production, Hypernuclei production, The coalescence model, Relativistic heavy ion collision

I. INTRODUCTION

In ultra-relativistic heavy ion collisions, light nuclei and hypernuclei such as the deuteron (d), helium-3 (^3He), triton (t), hypertriton (^3H), are a special group of observables [1–21]. They are composite clusters and their production mechanism is still under debate. The productions of such composite objects closely relate with many fundamental issues in relativistic heavy ion community, e.g., the hadronization mechanism [1], the hadronic rescattering effect [2], the structure of the quantum chromodynamics phase diagram [3–8], the local baryon-strangeness correlation [9, 10], the system freeze-out characteristic [11–16], the hyperon-nucleon interaction [17–19] and the search of more hadronic molecular states [20, 21].

In recent decades, the production of light nuclei and hypernuclei in ultra-relativistic heavy ion collisions has always attracted much attention both in experiment [22–35] and in theory [36–47]. The STAR experiment at the BNL Relativistic Heavy Ion Collider (RHIC) and the ALICE experiment at the CERN Large Hadron Collider (LHC) have put much effort into measurements of light nuclei [25–30] and hypernuclei [31–34]. In theory two production mechanisms, the thermal production mechanism [47–51] and the coalescence mechanism [40, 41, 52–61], have proved to be successful in describing formations of such composite objects.

The coalescence mechanism, in which light nuclei and hypernuclei are assumed to be produced by the coalescence of the jacent nucleons and hyperons in the phase space, possesses some unique characteristics [40, 41, 59–63]. To see whether, if so, to what extent, these characteristics depend on the particular coalescence models used in obtaining

these characteristics, we in our previous works [64–67] developed an analytical description for the production of different species of light nuclei. We applied the analytical nucleon coalescence model to Au+Au collisions at the RHIC to successfully explain the energy-dependent behaviors of d , t , ^3He and ^4He [64, 65]. We also applied it to pp, p+Pb, and Pb+Pb collisions at the LHC to understand the different behaviors of the coalescence factors B_2 and B_3 [66] from small to large collision systems, and gave a series of concise production correlations of d , ^3He and t [67].

Very recently, the ALICE collaboration published the most precise measurements to date of d , ^3He , t and especially ^3H in Pb+Pb collisions at $\sqrt{s_{NN}} = 5.02$ TeV [30, 33, 68]. In this work, we extend the coalescence model considering the coordinate-momentum correlation [67] to include the hyperon coalescence besides the nucleon coalescence and apply it to simultaneously study productions of light nuclei, the ^3H and different Ω -hypernuclei. One main goal of this article is to give an overall comprehension of the newest data in Pb+Pb collisions with the highest collision energy so far. The other goal is to bring production characteristics, especially production correlations, of light nuclei and hypernuclei originating from the coalescence itself to light. We propose two groups of interesting observables, the averaged transverse momentum ratios and centrality-dependent yield ratios of light nuclei to protons and hypernuclei to hyperons. These ratios happen to offset the differences of the primordial p , Λ , and Ω^- . This makes them powerful to reveal whether there exists a universal production mechanism for different species of nuclei in light and strange sectors. We find these ratios exhibit certain relations in the coalescence picture, which are very different from the thermal production mechanism.

The paper is organized as follows. In Sec. II, we introduce the coalescence model. We present the formulae of the momentum distributions of two baryons coalescing into dibaryon states and three baryons coalescing into tribaryon states, respectively. In Sec. III, we study behaviors of the coalescence factors B_2 and B_3 as functions of the

* Supported by the National Natural Science Foundation of China (No. 12175115 and No. 12375074)

† wangrq@qfnu.edu.cn

‡ songjun2011@jnxu.edu.cn

§ Corresponding author, shaofl@mail.sdu.edu.cn

69 collision centrality and the transverse momentum per nu-
70 cleon. We also study the transverse momentum (p_T) spec-
71 tra, the averaged transverse momenta $\langle p_T \rangle$, the yield rapid-
72 ity densities dN/dy and yield ratios of d , ${}^3\text{He}$ and \bar{t} . In
73 Sec. IV, we present results of the ${}^3_\Lambda\text{H}$ and Ω -hypernuclei.
74 We specially study the averaged transverse momentum ra-
75 tios $\frac{\langle p_T \rangle_d}{\langle p_T \rangle_p}$, $\frac{\langle p_T \rangle_{H(p\Omega^-)}}{\langle p_T \rangle_{\Omega^-}}$, $\frac{\langle p_T \rangle_{H(n\Omega^-)}}{\langle p_T \rangle_{\Omega^-}}$, $\frac{\langle p_T \rangle_t}{\langle p_T \rangle_p}$, $\frac{\langle p_T \rangle_{{}^3\text{He}}}{\langle p_T \rangle_p}$, $\frac{\langle p_T \rangle_{{}^3_\Lambda\text{H}}}{\langle p_T \rangle_\Lambda}$,
76 $\frac{\langle p_T \rangle_{H(pn\Omega^-)}}{\langle p_T \rangle_{\Omega^-}}$, and centrality-dependent behaviors of yield ra-
77 tios $\frac{d}{p}$, $\frac{H(p\Omega^-)}{\Omega^-}$, $\frac{H(n\Omega^-)}{\Omega^-}$, $\frac{t}{p}$, $\frac{{}^3\text{He}}{p}$, $\frac{{}^3_\Lambda\text{H}}{\Lambda}$, $\frac{H(pn\Omega^-)}{\Omega^-}$. In Sec. V,
78 we give our summary.

II. THE COALESCENCE MODEL

80 In this section, we extend the analytical nucleon coales-
81 cence model in our previous work [67] to include the hyperon
82 coalescence. In the current coalescence model, the coales-
83 cence process is executed on an equivalent kinetic freeze-out
84 surface formed from different times. To make the analyti-
85 cal and intuitive insights possible, we abandon carrying out
86 the time evolution step by step but absorb the finite emission
87 duration in an effective volume parameter. We first present
88 the formalism of two baryons coalescing into d -like dibaryon
89 states. We then give analytical expressions of three baryons
90 coalescing into ${}^3\text{He}$, t , and their partners in the strange sector.

A. Formalism of two bodies coalescing into dibaryon states

92 We begin with a hadronic system produced at the final
93 stage of the evolution of high energy collision, and suppose
94 the dibaryon state H_j is formed via the coalescence of two
95 baryons h_1 and h_2 . We use $f_{H_j}(\mathbf{p})$ to denote the three-
96 dimensional momentum distribution of the produced H_j and
97 it is given by

$$98 f_{H_j}(\mathbf{p}) = \int d\mathbf{x}_1 d\mathbf{x}_2 d\mathbf{p}_1 d\mathbf{p}_2 f_{h_1 h_2}(\mathbf{x}_1, \mathbf{x}_2; \mathbf{p}_1, \mathbf{p}_2) \\ \times \mathcal{R}_{H_j}(\mathbf{x}_1, \mathbf{x}_2; \mathbf{p}_1, \mathbf{p}_2), \quad (1)$$

100 where $f_{h_1 h_2}(\mathbf{x}_1, \mathbf{x}_2; \mathbf{p}_1, \mathbf{p}_2)$ is two-baryon joint coordinate-
101 momentum distribution; $\mathcal{R}_{H_j}(\mathbf{x}_1, \mathbf{x}_2; \mathbf{p}_1, \mathbf{p}_2, \mathbf{p})$ is the kernel
102 function of the H_j . Here and from now on we use bold sym-
103 bols to denote three-dimensional coordinate or momentum
104 vectors.

105 In terms of the normalized joint coordinate-momentum dis-
106 tribution denoted by the superscript '(n)', we have

$$107 f_{H_j}(\mathbf{p}) = N_{h_1 h_2} \int d\mathbf{x}_1 d\mathbf{x}_2 d\mathbf{p}_1 d\mathbf{p}_2 f_{h_1 h_2}^{(n)}(\mathbf{x}_1, \mathbf{x}_2; \mathbf{p}_1, \mathbf{p}_2) \\ \times \mathcal{R}_{H_j}(\mathbf{x}_1, \mathbf{x}_2; \mathbf{p}_1, \mathbf{p}_2, \mathbf{p}). \quad (2)$$

109 $N_{h_1 h_2} = N_{h_1} N_{h_2}$ is the number of all possible $h_1 h_2$ -pairs
110 in the considered hadronic system, and N_{h_i} ($i = 1, 2$) is the
111 number of the baryons h_i .

112 The kernel function $\mathcal{R}_{H_j}(\mathbf{x}_1, \mathbf{x}_2; \mathbf{p}_1, \mathbf{p}_2, \mathbf{p})$ denotes the
113 probability density for h_1, h_2 with momenta \mathbf{p}_1 and \mathbf{p}_2 at \mathbf{x}_1

114 and \mathbf{x}_2 to combine into an H_j of momentum \mathbf{p} . It carries the
115 kinetic and dynamical information of h_1 and h_2 combining
116 into H_j , and its precise expression should be constrained by
117 such as the momentum conservation, and constraints due to
118 intrinsic quantum numbers e.g., spin [64–67]. To take these
119 constraints into account explicitly, we rewrite the kernel func-
120 tion in the following form

$$121 \mathcal{R}_{H_j}(\mathbf{x}_1, \mathbf{x}_2; \mathbf{p}_1, \mathbf{p}_2, \mathbf{p}) = g_{H_j} \mathcal{R}_{H_j}^{(x,p)}(\mathbf{x}_1, \mathbf{x}_2; \mathbf{p}_1, \mathbf{p}_2) \\ \times \delta\left(\sum_{i=1}^2 \mathbf{p}_i - \mathbf{p}\right). \quad (3)$$

123 The spin degeneracy factor $g_{H_j} = (2J_{H_j} + 1)/[\prod_{i=1}^2 (2J_{h_i} + 1)]$, where J_{H_j} is the spin of the produced H_j and J_{h_i} is
125 that of the primordial baryon h_i . The Dirac δ function guar-
126antees the momentum conservation in the coalescence pro-
127 cess. The remaining $\mathcal{R}_{H_j}^{(x,p)}(\mathbf{x}_1, \mathbf{x}_2; \mathbf{p}_1, \mathbf{p}_2)$ can be solved
128 from the Wigner transformation as the H_j wave function is
129 given. Considering the wave function of a spherical harmonic
130 oscillator is particularly tractable and useful for analytical in-
131 sight, we adopt this profile as in Refs. [69–71] and have

$$132 \mathcal{R}_{H_j}^{(x,p)}(\mathbf{x}_1, \mathbf{x}_2; \mathbf{p}_1, \mathbf{p}_2) = 8e^{-\frac{(\mathbf{x}'_1 - \mathbf{x}'_2)^2}{2\sigma^2}} e^{-\frac{2\sigma^2(m_2 \mathbf{p}'_1 - m_1 \mathbf{p}'_2)^2}{(m_1 + m_2)^2}}. \quad (4)$$

133 The superscript ‘’ in the coordinate or momentum variables
134 denotes the baryon coordinate or momentum in the rest frame
135 of the $h_1 h_2$ -pair. m_1 and m_2 are the mass of h_1 and that of
136 h_2 . The width parameter $\sigma = \sqrt{\frac{2(m_1 + m_2)^2}{3(m_1^2 + m_2^2)}} R_{H_j}$, where R_{H_j}
137 is the root-mean-square radius of H_j .

138 Substituting Eqs. (3) and (4) into Eq. (2), we have

$$139 f_{H_j}(\mathbf{p}) = N_{h_1 h_2} g_{H_j} \int d\mathbf{x}_1 d\mathbf{x}_2 d\mathbf{p}_1 d\mathbf{p}_2 f_{h_1 h_2}^{(n)}(\mathbf{x}_1, \mathbf{x}_2; \mathbf{p}_1, \mathbf{p}_2) \\ \times 8e^{-\frac{(\mathbf{x}'_1 - \mathbf{x}'_2)^2}{2\sigma^2}} e^{-\frac{2\sigma^2(m_2 \mathbf{p}'_1 - m_1 \mathbf{p}'_2)^2}{(m_1 + m_2)^2}} \delta\left(\sum_{i=1}^2 \mathbf{p}_i - \mathbf{p}\right). \quad (5)$$

141 This is the general formalism of the H_j produced via the co-
142 alescence of two baryons h_1 and h_2 .

143 Noticing that the root-mean-square radius R_{H_j} of the d -
144 like dibaryon state H_j is always considered to be about or
145 larger than 2 fm, σ is even larger than R_{H_j} . So the gaus-
146 sian width in the momentum-dependent part of the kernel
147 function in Eq. (5) has a small value, about or smaller than
148 0.1 GeV. Therefore, we approximate the gaussian form of the
149 momentum-dependent kernel function to be a δ function form
150 as follows

$$151 e^{-\frac{(\mathbf{p}'_1 - \frac{m_1}{m_2} \mathbf{p}'_2)^2}{(1 + \frac{m_1}{m_2})^2 / (2\sigma^2)}} \approx \left[\frac{\sqrt{\pi}}{\sqrt{2}\sigma} \left(1 + \frac{m_1}{m_2}\right) \right]^3 \delta(\mathbf{p}'_1 - \frac{m_1}{m_2} \mathbf{p}'_2). \quad (6)$$

152 Substituting Eq. (6) into Eq. (5) and integrating \mathbf{p}_1 and \mathbf{p}_2 ,
153 we can obtain

$$154 f_{H_j}(\mathbf{p}) = N_{h_1 h_2} g_{H_j} \int d\mathbf{x}_1 d\mathbf{x}_2 d\mathbf{p}_1 d\mathbf{p}_2$$

$$\begin{aligned}
& f_{h_1 h_2}^{(n)}(\mathbf{x}_1, \mathbf{x}_2; \mathbf{p}_1, \mathbf{p}_2) 8 e^{-\frac{(\mathbf{x}'_1 - \mathbf{x}'_2)^2}{2\sigma^2}} \left(\frac{\sqrt{\pi}}{\sqrt{2}\sigma}\right)^3 (1 + \frac{m_1}{m_2})^3 \\
& \times \delta(\mathbf{p}'_1 - \frac{m_1}{m_2} \mathbf{p}'_2) \delta\left(\sum_{i=1}^2 \mathbf{p}_i - \mathbf{p}\right) \\
& = N_{h_1 h_2} g_{H_j} \int d\mathbf{x}_1 d\mathbf{x}_2 d\mathbf{p}_1 d\mathbf{p}_2 f_{h_1 h_2}^{(n)}(\mathbf{x}_1, \mathbf{x}_2; \mathbf{p}_1, \mathbf{p}_2) \\
& \times 8 e^{-\frac{(\mathbf{x}'_1 - \mathbf{x}'_2)^2}{2\sigma^2}} \left(\frac{\sqrt{\pi}}{\sqrt{2}\sigma}\right)^3 (1 + \frac{m_1}{m_2})^3 \gamma \delta(\mathbf{p}_1 - \frac{m_1}{m_2} \mathbf{p}_2) \\
& \times \delta\left(\sum_{i=1}^2 \mathbf{p}_i - \mathbf{p}\right) \\
& = N_{h_1 h_2} g_{H_j} \gamma \left(\frac{\sqrt{\pi}}{\sqrt{2}\sigma}\right)^3 \times 8 \int d\mathbf{x}_1 d\mathbf{x}_2 \\
& f_{h_1 h_2}^{(n)}(\mathbf{x}_1, \mathbf{x}_2; \frac{m_1 \mathbf{p}}{m_1 + m_2}, \frac{m_2 \mathbf{p}}{m_1 + m_2}) e^{-\frac{(\mathbf{x}'_1 - \mathbf{x}'_2)^2}{2\sigma^2}}. \quad (7)
\end{aligned}$$

The γ is the Lorentz contraction factor corresponding to the three-dimensional velocity β of the center-of-mass frame of $h_1 h_2$ -pair in the laboratory frame. Here the momentum Lorentz transformation is $\mathbf{p}'_{1//} - \frac{m_1}{m_2} \mathbf{p}'_{2//} = \frac{1}{\gamma}(\mathbf{p}_{1//} - \frac{m_1}{m_2} \mathbf{p}_{2//})$ and $\mathbf{p}'_{1\perp} - \frac{m_1}{m_2} \mathbf{p}'_{2\perp} = \mathbf{p}_{1\perp} - \frac{m_1}{m_2} \mathbf{p}_{2\perp}$. The subscript ‘//’ denotes the direction parallel to β and ‘ \perp ’ perpendicular to it.

Changing coordinate variables in Eq. (7) to be $\mathbf{X} = \frac{m_1 \mathbf{x}_1 + m_2 \mathbf{x}_2}{\sqrt{2}(m_1 + m_2)}$ and $\mathbf{r} = \frac{\mathbf{x}_1 - \mathbf{x}_2}{\sqrt{2}}$, we have

$$\begin{aligned}
f_{H_j}(\mathbf{p}) &= N_{h_1 h_2} g_{H_j} \gamma \left(\frac{\sqrt{\pi}}{\sqrt{2}\sigma}\right)^3 \times \\
& 8 \int d\mathbf{X} d\mathbf{r} f_{h_1 h_2}^{(n)}(\mathbf{X}, \mathbf{r}; \frac{m_1 \mathbf{p}}{m_1 + m_2}, \frac{m_2 \mathbf{p}}{m_1 + m_2}) e^{-\frac{r'^2}{\sigma^2}}. \quad (8)
\end{aligned}$$

Considering the strong interaction and the coalescence are local, we neglect the effect of collective motion on the center of mass coordinate and assume it is factorized, i.e.,

$$\begin{aligned}
f_{h_1 h_2}^{(n)}(\mathbf{X}, \mathbf{r}; \frac{m_1 \mathbf{p}}{m_1 + m_2}, \frac{m_2 \mathbf{p}}{m_1 + m_2}) &= f_{h_1 h_2}^{(n)}(\mathbf{X}) \\
&\times f_{h_1 h_2}^{(n)}(\mathbf{r}; \frac{m_1 \mathbf{p}}{m_1 + m_2}, \frac{m_2 \mathbf{p}}{m_1 + m_2}). \quad (9)
\end{aligned}$$

Substituting Eq. (9) into Eq. (8), we have

$$\begin{aligned}
f_{H_j}(\mathbf{p}) &= N_{h_1 h_2} g_{H_j} \gamma \left(\frac{\sqrt{\pi}}{\sqrt{2}\sigma}\right)^3 \\
&\times 8 \int d\mathbf{r} f_{h_1 h_2}^{(n)}(\mathbf{r}; \frac{m_1 \mathbf{p}}{m_1 + m_2}, \frac{m_2 \mathbf{p}}{m_1 + m_2}) e^{-\frac{r'^2}{\sigma^2}}. \quad (10)
\end{aligned}$$

We adopt the frequently-used gaussian form for the relative

$$\begin{aligned}
& \text{coordinate distribution as in such as Refs. [72–74], i.e.,} \\
& f_{h_1 h_2}^{(n)}(\mathbf{r}; \frac{m_1 \mathbf{p}}{m_1 + m_2}, \frac{m_2 \mathbf{p}}{m_1 + m_2}) = \frac{1}{\left[\pi C_0 R_f^2(\mathbf{p})\right]^{3/2}} \\
& \times e^{-\frac{\mathbf{r}^2}{C_0 R_f^2(\mathbf{p})}} f_{h_1 h_2}^{(n)}\left(\frac{m_1 \mathbf{p}}{m_1 + m_2}, \frac{m_2 \mathbf{p}}{m_1 + m_2}\right). \quad (11)
\end{aligned}$$

Here $R_f(\mathbf{p})$ is the effective radius of the hadronic source system at the H_j freeze-out. C_0 is introduced to make \mathbf{r}^2/C_0 to be the square of one-half of the relative position and it is 2 [72–74]. In this way $R_f(\mathbf{p})$ is just the Hanbury-Brown-Twiss (HBT) interferometry radius, which can also be extracted from the two-particle femtoscopic correlations [73, 74].

With instantaneous coalescence in the rest frame of $h_1 h_2$ -pair, i.e., $\Delta t' = 0$, we get the coordinate Lorentz transformation

$$\mathbf{r} = \mathbf{r}' + (\gamma - 1) \frac{\mathbf{r}' \cdot \beta}{\beta^2} \beta. \quad (12)$$

Substituting Eq. (11) into Eq. (10) and using Eq. (12) to integrate from the relative coordinate variable, we obtain

$$\begin{aligned}
f_{H_j}(\mathbf{p}) &= \frac{8\pi^{3/2} g_{H_j} \gamma}{2^{3/2} \left[C_0 R_f^2(\mathbf{p}) + \sigma^2\right] \sqrt{C_0 [R_f(\mathbf{p})/\gamma]^2 + \sigma^2}} \\
&\times f_{h_1 h_2}\left(\frac{m_1 \mathbf{p}}{m_1 + m_2}, \frac{m_2 \mathbf{p}}{m_1 + m_2}\right). \quad (13)
\end{aligned}$$

Ignoring correlations between h_1 and h_2 , we have the three-dimensional momentum distribution of the H_j as

$$\begin{aligned}
f_{H_j}(\mathbf{p}) &= \frac{8\pi^{3/2} g_{H_j} \gamma}{2^{3/2} \left[C_0 R_f^2(\mathbf{p}) + \sigma^2\right] \sqrt{C_0 [R_f(\mathbf{p})/\gamma]^2 + \sigma^2}} \\
&\times f_{h_1}\left(\frac{m_1 \mathbf{p}}{m_1 + m_2}\right) f_{h_2}\left(\frac{m_2 \mathbf{p}}{m_1 + m_2}\right). \quad (14)
\end{aligned}$$

Denoting the Lorentz invariant momentum distribution $E \frac{d^3 N}{d\mathbf{p}^3} = \frac{d^2 N}{2\pi p_T d p_T dy}$ with $f^{(inv)}$, we finally have

$$\begin{aligned}
f_{H_j}^{(inv)}(p_T, y) &= \frac{8\pi^{3/2} g_{H_j}}{2^{3/2} \left[C_0 R_f^2(p_T, y) + \sigma^2\right] \sqrt{C_0 \frac{R_f^2(p_T, y)}{\gamma^2} + \sigma^2}} \\
&\times \frac{m_{H_j}}{m_1 m_2} f_{h_1}^{(inv)}\left(\frac{m_1 p_T}{m_1 + m_2}, y\right) f_{h_2}^{(inv)}\left(\frac{m_2 p_T}{m_1 + m_2}, y\right), \quad (15)
\end{aligned}$$

where y is the longitudinal rapidity and m_{H_j} is the mass of the H_j .

B. Formalism of three bodies coalescing into tribaryon states

210 For tribaryon state H_j formed via the coalescence of three baryons h_1, h_2 and h_3 , the momentum distribution $f_{H_j}(\mathbf{p})$ is

$$211 \quad f_{H_j}(\mathbf{p}) = N_{h_1 h_2 h_3} \int d\mathbf{x}_1 d\mathbf{x}_2 d\mathbf{x}_3 d\mathbf{p}_1 d\mathbf{p}_2 d\mathbf{p}_3 f_{h_1 h_2 h_3}^{(n)}(\mathbf{x}_1, \mathbf{x}_2, \mathbf{x}_3; \mathbf{p}_1, \mathbf{p}_2, \mathbf{p}_3) \mathcal{R}_{H_j}(\mathbf{x}_1, \mathbf{x}_2, \mathbf{x}_3; \mathbf{p}_1, \mathbf{p}_2, \mathbf{p}_3, \mathbf{p}). \quad (16)$$

212 $N_{h_1 h_2 h_3}$ is the number of all possible $h_1 h_2 h_3$ -clusters and it equals to $N_{h_1} N_{h_2} N_{h_3}$, $N_{h_1} (N_{h_1} - 1) N_{h_3}$ for $h_1 \neq h_2 \neq h_3$,
213 $h_1 = h_2 \neq h_3$, respectively. $f_{h_1 h_2 h_3}^{(n)}(\mathbf{x}_1, \mathbf{x}_2, \mathbf{x}_3; \mathbf{p}_1, \mathbf{p}_2, \mathbf{p}_3)$ is the normalized three-baryon joint coordinate-momentum
214 distribution, and $\mathcal{R}_{H_j}(\mathbf{x}_1, \mathbf{x}_2, \mathbf{x}_3; \mathbf{p}_1, \mathbf{p}_2, \mathbf{p}_3, \mathbf{p})$ is the kernel function.

215 We rewrite the kernel function as

$$216 \quad \mathcal{R}_{H_j}(\mathbf{x}_1, \mathbf{x}_2, \mathbf{x}_3; \mathbf{p}_1, \mathbf{p}_2, \mathbf{p}_3, \mathbf{p}) = g_{H_j} \mathcal{R}_{H_j}^{(x,p)}(\mathbf{x}_1, \mathbf{x}_2, \mathbf{x}_3; \mathbf{p}_1, \mathbf{p}_2, \mathbf{p}_3) \delta\left(\sum_{i=1}^3 \mathbf{p}_i - \mathbf{p}\right). \quad (17)$$

217 The spin degeneracy factor $g_{H_j} = (2J_{H_j} + 1)/[\prod_{i=1}^3 (2J_{h_i} + 1)]$. The Dirac δ function guarantees the momentum conservation.

218 $\mathcal{R}_{H_j}^{(x,p)}(\mathbf{x}_1, \mathbf{x}_2, \mathbf{x}_3; \mathbf{p}_1, \mathbf{p}_2, \mathbf{p}_3)$ solving from the Wigner transformation [69–71] is

$$219 \quad \mathcal{R}_{H_j}^{(x,p)}(\mathbf{x}_1, \mathbf{x}_2, \mathbf{x}_3; \mathbf{p}_1, \mathbf{p}_2, \mathbf{p}_3) = 8^2 e^{-\frac{(\mathbf{x}'_1 - \mathbf{x}'_2)^2}{2\sigma_1^2}} e^{-\frac{2(\frac{m_1 \mathbf{x}'_1}{m_1 + m_2} + \frac{m_2 \mathbf{x}'_2}{m_1 + m_2} - \mathbf{x}'_3)^2}{3\sigma_2^2}} e^{-\frac{2\sigma_1^2(m_2 \mathbf{p}'_1 - m_1 \mathbf{p}'_2)^2}{(m_1 + m_2)^2}} e^{-\frac{3\sigma_2^2[m_3 \mathbf{p}'_1 + m_3 \mathbf{p}'_2 - (m_1 + m_2) \mathbf{p}'_3]^2}{2(m_1 + m_2 + m_3)^2}}. \quad (18)$$

220 The superscript “ \prime ” denotes the baryon coordinate or momentum in the rest frame of the $h_1 h_2 h_3$ -
221 cluster. The width parameter $\sigma_1 = \sqrt{\frac{m_3(m_1 + m_2)(m_1 + m_2 + m_3)}{m_1 m_2(m_1 + m_2) + m_2 m_3(m_2 + m_3) + m_3 m_1(m_3 + m_1)}} R_{H_j}$, and $\sigma_2 =$
222 $\sqrt{\frac{4m_1 m_2(m_1 + m_2 + m_3)^2}{3(m_1 + m_2)[m_1 m_2(m_1 + m_2) + m_2 m_3(m_2 + m_3) + m_3 m_1(m_3 + m_1)]}} R_{H_j}$.

223 Substituting Eqs. (17) and (18) into Eq. (16), we have

$$224 \quad f_{H_j}(\mathbf{p}) = 8^2 N_{h_1 h_2 h_3} g_{H_j} \int d\mathbf{x}_1 d\mathbf{x}_2 d\mathbf{x}_3 d\mathbf{p}_1 d\mathbf{p}_2 d\mathbf{p}_3 e^{-\frac{(\mathbf{x}'_1 - \mathbf{x}'_2)^2}{2\sigma_1^2}} e^{-\frac{2(\frac{m_1 \mathbf{x}'_1}{m_1 + m_2} + \frac{m_2 \mathbf{x}'_2}{m_1 + m_2} - \mathbf{x}'_3)^2}{3\sigma_2^2}} f_{h_1 h_2 h_3}^{(n)}(\mathbf{x}_1, \mathbf{x}_2, \mathbf{x}_3; \mathbf{p}_1, \mathbf{p}_2, \mathbf{p}_3) \\ 225 \quad \times e^{-\frac{2\sigma_1^2(m_2 \mathbf{p}'_1 - m_1 \mathbf{p}'_2)^2}{(m_1 + m_2)^2}} e^{-\frac{3\sigma_2^2[m_3 \mathbf{p}'_1 + m_3 \mathbf{p}'_2 - (m_1 + m_2) \mathbf{p}'_3]^2}{2(m_1 + m_2 + m_3)^2}} \delta\left(\sum_{i=1}^3 \mathbf{p}_i - \mathbf{p}\right). \quad (19)$$

226 Approximating the gaussian form of the momentum-dependent kernel function to be δ function form and integrating $\mathbf{p}_1, \mathbf{p}_2$
227 and \mathbf{p}_3 from Eq. (19), we can obtain

$$228 \quad f_{H_j}(\mathbf{p}) = 8^2 N_{h_1 h_2 h_3} g_{H_j} \int d\mathbf{x}_1 d\mathbf{x}_2 d\mathbf{x}_3 d\mathbf{p}_1 d\mathbf{p}_2 d\mathbf{p}_3 f_{h_1 h_2 h_3}^{(n)}(\mathbf{x}_1, \mathbf{x}_2, \mathbf{x}_3; \mathbf{p}_1, \mathbf{p}_2, \mathbf{p}_3) e^{-\frac{(\mathbf{x}'_1 - \mathbf{x}'_2)^2}{2\sigma_1^2}} e^{-\frac{2(\frac{m_1 \mathbf{x}'_1}{m_1 + m_2} + \frac{m_2 \mathbf{x}'_2}{m_1 + m_2} - \mathbf{x}'_3)^2}{3\sigma_2^2}} \\ 229 \quad \times \left(\frac{\sqrt{\pi}}{\sqrt{2}\sigma_1}\right)^3 \left(1 + \frac{m_1}{m_2}\right)^3 \delta(\mathbf{p}'_1 - \frac{m_1}{m_2} \mathbf{p}'_2) \left(\frac{\sqrt{2\pi}}{\sqrt{3}\sigma_2}\right)^3 \left(1 + \frac{m_1}{m_3} + \frac{m_2}{m_3}\right)^3 \delta(\mathbf{p}'_1 + \mathbf{p}'_2 - \frac{m_1 + m_2}{m_3} \mathbf{p}'_3) \delta\left(\sum_{i=1}^3 \mathbf{p}_i - \mathbf{p}\right) \\ 230 \quad = 8^2 N_{h_1 h_2 h_3} g_{H_j} \int d\mathbf{x}_1 d\mathbf{x}_2 d\mathbf{x}_3 d\mathbf{p}_1 d\mathbf{p}_2 d\mathbf{p}_3 f_{h_1 h_2 h_3}^{(n)}(\mathbf{x}_1, \mathbf{x}_2, \mathbf{x}_3; \mathbf{p}_1, \mathbf{p}_2, \mathbf{p}_3) e^{-\frac{(\mathbf{x}'_1 - \mathbf{x}'_2)^2}{2\sigma_1^2}} e^{-\frac{2(\frac{m_1 \mathbf{x}'_1}{m_1 + m_2} + \frac{m_2 \mathbf{x}'_2}{m_1 + m_2} - \mathbf{x}'_3)^2}{3\sigma_2^2}} \\ 231 \quad \times \left(\frac{\sqrt{\pi}}{\sqrt{2}\sigma_1}\right)^3 \left(1 + \frac{m_1}{m_2}\right)^3 \gamma \delta(\mathbf{p}_1 - \frac{m_1}{m_2} \mathbf{p}_2) \left(\frac{\sqrt{2\pi}}{\sqrt{3}\sigma_2}\right)^3 \left(1 + \frac{m_1}{m_3} + \frac{m_2}{m_3}\right)^3 \gamma \delta(\mathbf{p}_1 + \mathbf{p}_2 - \frac{m_1 + m_2}{m_3} \mathbf{p}_3) \delta\left(\sum_{i=1}^3 \mathbf{p}_i - \mathbf{p}\right) \\ 232 \quad = 8^2 N_{h_1 h_2 h_3} g_{H_j} \gamma^2 \left(\frac{\pi}{\sqrt{3}\sigma_1\sigma_2}\right)^3 \int d\mathbf{x}_1 d\mathbf{x}_2 d\mathbf{x}_3 f_{h_1 h_2 h_3}^{(n)}(\mathbf{x}_1, \mathbf{x}_2, \mathbf{x}_3; \frac{m_1 \mathbf{p}}{m_1 + m_2 + m_3}, \frac{m_2 \mathbf{p}}{m_1 + m_2 + m_3}, \frac{m_3 \mathbf{p}}{m_1 + m_2 + m_3}) \\ 233 \quad \times e^{-\frac{(\mathbf{x}'_1 - \mathbf{x}'_2)^2}{2\sigma_1^2}} e^{-\frac{2(\frac{m_1 \mathbf{x}'_1}{m_1 + m_2} + \frac{m_2 \mathbf{x}'_2}{m_1 + m_2} - \mathbf{x}'_3)^2}{3\sigma_2^2}}. \quad (20)$$

234 Changing coordinate variables in Eq. (20) to be $\mathbf{Y} = (m_1 \mathbf{x}_1 + m_2 \mathbf{x}_2 + m_3 \mathbf{x}_3)/(m_1 + m_2 + m_3)$, $\mathbf{r}_1 = (\mathbf{x}_1 - \mathbf{x}_2)/\sqrt{2}$ and
235 $\mathbf{r}_2 = \sqrt{\frac{2}{3}}(\frac{m_1 \mathbf{x}_1}{m_1 + m_2} + \frac{m_2 \mathbf{x}_2}{m_1 + m_2} - \mathbf{x}_3)$ as in Refs. [69–71], we have

$$236 \quad f_{H_j}(\mathbf{p}) = 8^2 N_{h_1 h_2 h_3} g_{H_j} \gamma^2 \left(\frac{\pi}{\sqrt{3}\sigma_1\sigma_2}\right)^3$$

$$237 \quad \times \int 3^{3/2} d\mathbf{Y} d\mathbf{r}_1 d\mathbf{r}_2 f_{h_1 h_2 h_3}^{(n)}(\mathbf{Y}, \mathbf{r}_1, \mathbf{r}_2; \frac{m_1 \mathbf{p}}{m_1 + m_2 + m_3}, \frac{m_2 \mathbf{p}}{m_1 + m_2 + m_3}, \frac{m_3 \mathbf{p}}{m_1 + m_2 + m_3}) e^{-\frac{r_1'^2}{\sigma_1^2}} e^{-\frac{r_2'^2}{\sigma_2^2}}. \quad (21)$$

238 We also assume the center of mass coordinate in joint distribution is factorized, i.e.,

$$239 \quad 3^{3/2} f_{h_1 h_2 h_3}^{(n)}(\mathbf{Y}, \mathbf{r}_1, \mathbf{r}_2; \frac{m_1 \mathbf{p}}{m_1 + m_2 + m_3}, \frac{m_2 \mathbf{p}}{m_1 + m_2 + m_3}, \frac{m_3 \mathbf{p}}{m_1 + m_2 + m_3}) \\ 240 \quad = f_{h_1 h_2 h_3}^{(n)}(\mathbf{Y}) f_{h_1 h_2 h_3}^{(n)}(\mathbf{r}_1, \mathbf{r}_2; \frac{m_1 \mathbf{p}}{m_1 + m_2 + m_3}, \frac{m_2 \mathbf{p}}{m_1 + m_2 + m_3}, \frac{m_3 \mathbf{p}}{m_1 + m_2 + m_3}). \quad (22)$$

241 Substituting Eq. (22) into Eq. (21), we have

$$242 \quad f_{H_j}(\mathbf{p}) = 8^2 N_{h_1 h_2 h_3} g_{H_j} \gamma^2 \left(\frac{\pi}{\sqrt{3} \sigma_1 \sigma_2} \right)^3 \int d\mathbf{r}_1 d\mathbf{r}_2 f_{h_1 h_2 h_3}^{(n)}(\mathbf{r}_1, \mathbf{r}_2; \frac{m_1 \mathbf{p}}{m_1 + m_2 + m_3}, \frac{m_2 \mathbf{p}}{m_1 + m_2 + m_3}, \frac{m_3 \mathbf{p}}{m_1 + m_2 + m_3}) \\ 243 \quad \times e^{-\frac{r_1'^2}{\sigma_1^2}} e^{-\frac{r_2'^2}{\sigma_2^2}}. \quad (23)$$

244 Adopting gaussian forms for the relative coordinate distributions [66, 72–74], we have

$$245 \quad f_{h_1 h_2 h_3}^{(n)}(\mathbf{r}_1, \mathbf{r}_2; \frac{m_1 \mathbf{p}}{m_1 + m_2 + m_3}, \frac{m_2 \mathbf{p}}{m_1 + m_2 + m_3}, \frac{m_3 \mathbf{p}}{m_1 + m_2 + m_3}) \\ 246 \quad = \frac{1}{[\pi C_1 R_f^2(\mathbf{p})]^{3/2}} e^{-\frac{r_1^2}{C_1 R_f^2(\mathbf{p})}} \frac{1}{[\pi C_2 R_f^2(\mathbf{p})]^{3/2}} e^{-\frac{r_2^2}{C_2 R_f^2(\mathbf{p})}} f_{h_1 h_2 h_3}^{(n)}(\frac{m_1 \mathbf{p}}{m_1 + m_2 + m_3}, \frac{m_2 \mathbf{p}}{m_1 + m_2 + m_3}, \frac{m_3 \mathbf{p}}{m_1 + m_2 + m_3}). \quad (24)$$

247 Comparing relations of $\mathbf{r}_1, \mathbf{r}_2$ with $\mathbf{x}_1, \mathbf{x}_2, \mathbf{x}_3$ to that of \mathbf{r} with $\mathbf{x}_1, \mathbf{x}_2$ in Sec. II A, we see that C_1 is equal to C_0 and C_2 is
248 $4C_0/3$ [66, 72–74]. Substituting Eq. (24) into Eq. (23) and considering the coordinate Lorentz transformation, we integrate
249 from the relative coordinate variables and obtain

$$250 \quad f_{H_j}(\mathbf{p}) = \frac{8^2 \pi^3 g_{H_j} \gamma^2}{3^{3/2} [C_1 R_f^2(\mathbf{p}) + \sigma_1^2] \sqrt{C_1 [R_f(\mathbf{p})/\gamma]^2 + \sigma_1^2} [C_2 R_f^2(\mathbf{p}) + \sigma_2^2] \sqrt{C_2 [R_f(\mathbf{p})/\gamma]^2 + \sigma_2^2}} \\ 251 \quad \times f_{h_1 h_2 h_3}(\frac{m_1 \mathbf{p}}{m_1 + m_2 + m_3}, \frac{m_2 \mathbf{p}}{m_1 + m_2 + m_3}, \frac{m_3 \mathbf{p}}{m_1 + m_2 + m_3}). \quad (25)$$

252 Ignoring correlations between h_1, h_2 and h_3 , we have the three-dimensional momentum distribution of H_j as

$$253 \quad f_{H_j}(\mathbf{p}) = \frac{8^2 \pi^3 g_{H_j} \gamma^2}{3^{3/2} [C_1 R_f^2(\mathbf{p}) + \sigma_1^2] \sqrt{C_1 [R_f(\mathbf{p})/\gamma]^2 + \sigma_1^2} [C_2 R_f^2(\mathbf{p}) + \sigma_2^2] \sqrt{C_2 [R_f(\mathbf{p})/\gamma]^2 + \sigma_2^2}} \\ 254 \quad \times f_{h_1}(\frac{m_1 \mathbf{p}}{m_1 + m_2 + m_3}) f_{h_2}(\frac{m_2 \mathbf{p}}{m_1 + m_2 + m_3}) f_{h_3}(\frac{m_3 \mathbf{p}}{m_1 + m_2 + m_3}). \quad (26)$$

255 Finally, we have the Lorentz invariant momentum distribution as

$$256 \quad f_{H_j}^{(inv)}(p_T, y) = \frac{8^2 \pi^3 g_{H_j}}{3^{3/2} [C_1 R_f^2(p_T, y) + \sigma_1^2] \sqrt{C_1 [R_f(p_T, y)/\gamma]^2 + \sigma_1^2} [C_2 R_f^2(p_T, y) + \sigma_2^2] \sqrt{C_2 [R_f(p_T, y)/\gamma]^2 + \sigma_2^2}} \\ 257 \quad \times \frac{m_{H_j}}{m_1 m_2 m_3} f_{h_1}^{(inv)}(\frac{m_1 p_T}{m_1 + m_2 + m_3}, y) f_{h_2}^{(inv)}(\frac{m_2 p_T}{m_1 + m_2 + m_3}, y) f_{h_3}^{(inv)}(\frac{m_3 p_T}{m_1 + m_2 + m_3}, y). \quad (27)$$

258 As a short summary of this section, we want to state that 266 ular states. And what's more, they can be conveniently used
259 Eqs. (15) and (27) give: (i) the relationships of dibaryon states 267 to investigate production correlations of different species of
260 and tribaryon states with primordial baryons in momentum 268 composite objects. Formulae for the antiparticles are the same
261 space in the laboratory frame, (ii) effects of different fac- 269 as these dibaryon and tribaryon states, and we leave out the
262 tors on dibaryon or tribaryon production such as the whole 270 duplication. Their applications at midrapidity (i.e., $y = 0$) in
263 hadronic system scale and the size of the formed composite 271 heavy ion collisions at the LHC will be shown in the follow-
264 object. They can be directly used to calculate the productions 272 ing sections.
265 of light nuclei, hypernuclei, and even other hadronic molec-

273

III. RESULTS OF LIGHT NUCLEI

274 In this section, we use the coalescence model to study produc-
 275 tions of d , ${}^3\text{He}$ and t at midrapidity in $\text{Pb}+\text{Pb}$ collisions at
 276 $\sqrt{s_{NN}} = 5.02$ TeV. We first calculate the coalescence factors
 277 B_2 , B_3 and discuss their centrality and p_T -dependent behav-
 278 iors. We then compute the p_T spectra of d , ${}^3\text{He}$ and t . We
 279 finally calculate the averaged transverse momenta $\langle p_T \rangle$, the
 280 yield rapidity densities dN/dy and the yield ratios of differ-
 281 ent light nuclei.

282 A. The coalescence factor of light nuclei

283 The coalescence factor B_A is defined as

$$284 B_A(p_T) = \frac{f_{d,{}^3\text{He},t}^{(inv)}(p_T)}{\left[f_p^{(inv)}(\frac{p_T}{A})\right]^Z \left[f_n^{(inv)}(\frac{p_T}{A})\right]^{A-Z}}, \quad (28)$$

285 where A is the mass number and Z is the charge of the light
 286 nuclei. It is a unique link between the formed light nuclei
 287 and the primordial nucleons, and much effort has been put
 288 into B_A in different coalescence models [11, 13, 57–59, 75].
 289 From Eqs. (15) and (27), we respectively have for d , ${}^3\text{He}$ and
 290 t

$$291 B_2(p_T) = \frac{m_d g_d (\sqrt{2\pi})^3}{m_p m_n \left[C_0 R_f^2(p_T) + \sigma_d^2\right] \sqrt{C_0 \left[\frac{R_f(p_T)}{\gamma}\right]^2 + \sigma_d^2}}, \quad (29)$$

$$293 B_3(p_T) = \frac{64\pi^3 g_3^{} \text{He}}{3^{\frac{3}{2}} \left[C_1 R_f^2(p_T) + \sigma_3^2 \text{He}\right] \sqrt{C_1 \left[\frac{R_f(p_T)}{\gamma}\right]^2 + \sigma_3^2 \text{He}}} \\ 294 \times \frac{m_3^{} \text{He}}{m_p^2 m_n \left[C_2 R_f^2(p_T) + \sigma_3^2 \text{He}\right] \sqrt{C_2 \left[\frac{R_f(p_T)}{\gamma}\right]^2 + \sigma_3^2 \text{He}}}, \quad (30)$$

$$295 B_3(p_T) = \frac{64\pi^3 g_t}{3^{\frac{3}{2}} \left[C_1 R_f^2(p_T) + \sigma_t^2\right] \sqrt{C_1 \left[\frac{R_f(p_T)}{\gamma}\right]^2 + \sigma_t^2}} \\ 296 \times \frac{m_t}{m_p m_n^2 \left[C_2 R_f^2(p_T) + \sigma_t^2\right] \sqrt{C_2 \left[\frac{R_f(p_T)}{\gamma}\right]^2 + \sigma_t^2}}. \quad (31)$$

297 Here $\sigma_d = \sqrt{\frac{4}{3}} R_d$, and the root-mean-square radius of the
 298 deuteron $R_d = 2.1421$ fm [76]. $\sigma_3^{} \text{He} = R_3^{} \text{He} = 1.9661$ fm
 299 and $\sigma_t = R_t = 1.7591$ fm [76]. $m_{p,n}$ denotes the nucleon
 300 mass and $m_{d,{}^3\text{He},t}$ the mass of the d , ${}^3\text{He}$ or t .

301 To further compute B_2 and B_3 , the specific form of
 302 $R_f(p_T)$ is necessary. Similar to Ref. [67], the dependence
 303 of $R_f(p_T)$ on centrality and p_T is considered to factorize into
 304 a linear dependence on the cube root of the pseudorapidity
 305 density of charged particles $(dN_{ch}/d\eta)^{1/3}$ and a power-law
 306 dependence on the transverse mass of the formed light nu-
 307 cleus m_T [74]. So we have

$$308 R_f(p_T) = a \times (dN_{ch}/d\eta)^{\frac{1}{3}} \times \left(\sqrt{p_T^2 + m_{d,{}^3\text{He},t}^2}\right)^b, \quad (32)$$

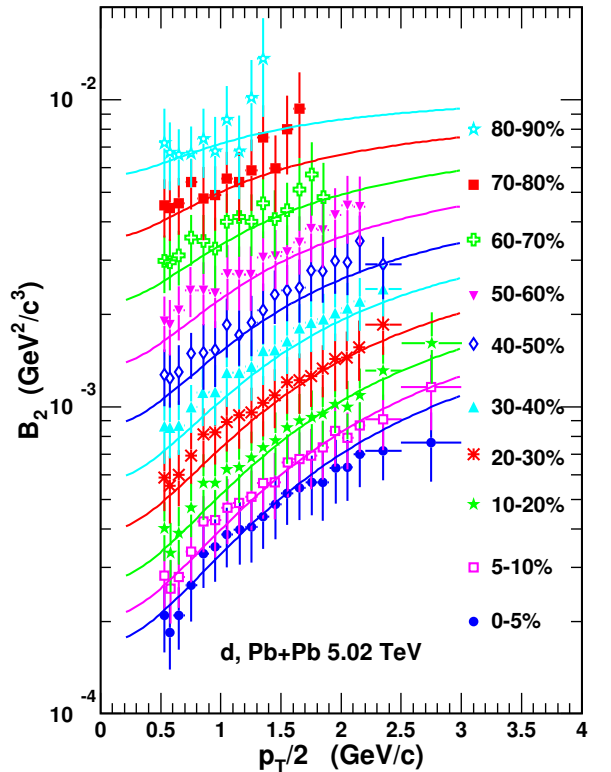


Fig. 1. The B_2 of d as a function of $p_T/2$ in different centralities in $\text{Pb}+\text{Pb}$ collisions at $\sqrt{s_{NN}} = 5.02$ TeV. Symbols with error bars are experimental data [77] and solid lines are theoretical results.

309 where a and b are free parameters. Their values in $\text{Pb}+\text{Pb}$
 310 collisions at $\sqrt{s_{NN}} = 5.02$ TeV are $(0.70, -0.31)$ for d and
 311 $(0.66, -0.31)$ for ${}^3\text{He}$ and t , which are determined by repro-
 312 ducing the data of the p_T spectra of d and ${}^3\text{He}$ in the most
 313 central 0-5% centrality. Here b is set to be centrality inde-
 314 pendent, which is consistent with that in hydrodynamics [78]
 315 and that in STAR measurements of two-pion interferometry
 316 in central and semi-central $\text{Au}+\text{Au}$ collisions [79]. a is also
 317 set to be centrality-independent, the same as that in our pre-
 318 vious work [67].

319 We use the data of $dN_{ch}/d\eta$ in Ref. [80] to evaluate
 320 $R_f(p_T)$, and then compute coalescence factors B_2 and B_3 .
 321 Fig. 1 shows B_2 of d as a function of the transverse momen-
 322 tum scaled by the mass number $p_T/2$ in different centralities
 323 in $\text{Pb}+\text{Pb}$ collisions at $\sqrt{s_{NN}} = 5.02$ TeV. Symbols with er-
 324 ror bars are experimental data [77] and solid lines are the-
 325 oretical results of the coalescence model. From Fig. 1, one
 326 can see from central to peripheral collisions B_2 exhibits an
 327 increasing trend, which is due to the decreasing scale of the
 328 created hadronic system. For a certain centrality, B_2 increases
 329 as a function of $p_T/2$. This increased behavior results on one
 330 hand from the Lorentz contraction factor γ , which has been
 331 studied in Ref. [66]. On the other hand, it results from the
 332 decreasing R_f with increasing p_T . The rising behavior of
 333 the experimental data as a function of $p_T/2$ from central to
 334 peripheral collisions can be quantitatively described by the co-
 335 alescence model.

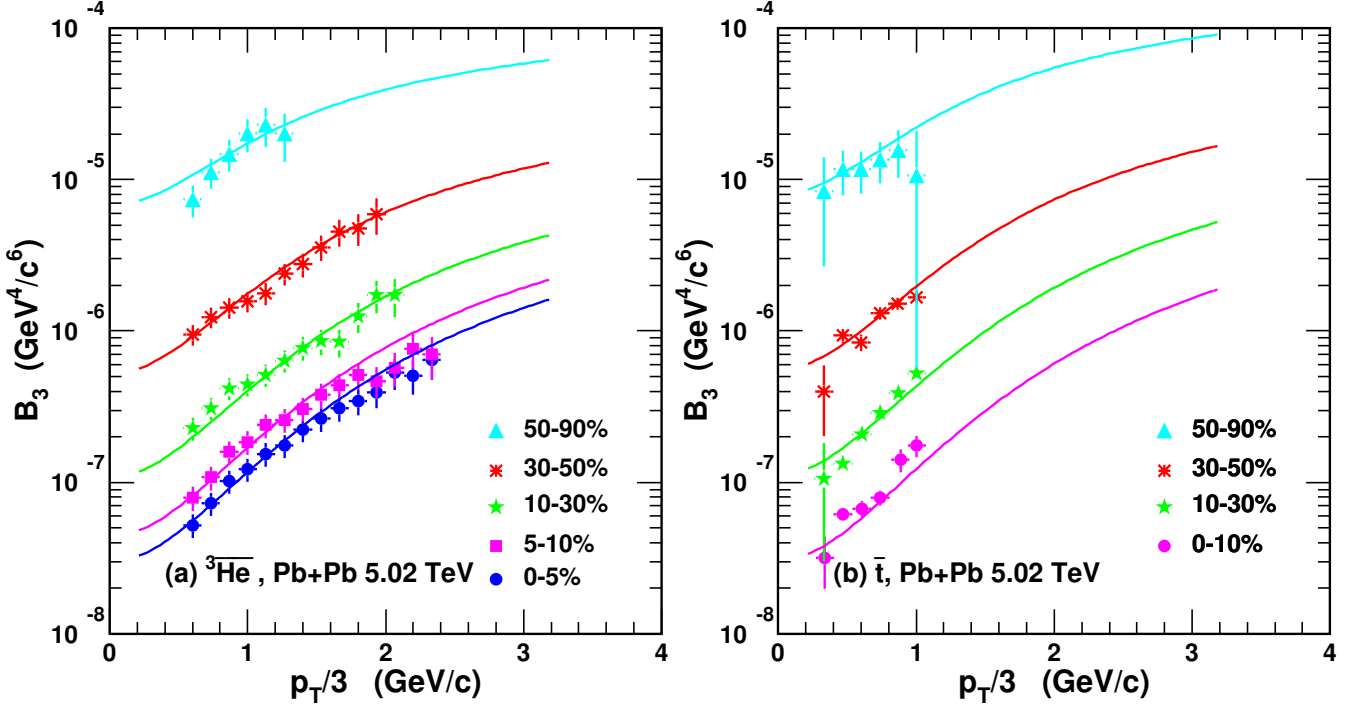


Fig. 2. The B_3 of (a) ${}^3\text{He}$ and (b) \bar{t} as a function of $p_T/3$ in different centralities in Pb+Pb collisions at $\sqrt{s_{NN}} = 5.02 \text{ TeV}$. Symbols with error bars are experimental data [30] and solid lines are theoretical results.

Fig. 2 shows B_3 of ${}^3\text{He}$ and that of \bar{t} as a function of $p_T/3$ in different centralities in Pb+Pb collisions at $\sqrt{s_{NN}} = 5.02 \text{ TeV}$. Symbols with error bars are experimental data [30] and solid lines are theoretical results. Similarly, as B_2 , experimental data of B_3 also exhibit a rising trend as a function of $p_T/3$, which is reproduced well by the coalescence model from central to peripheral collisions. Fig. 1 and Fig. 2 show that the centrality and momentum-dependent behaviors of B_2 and B_3 in Pb+Pb collisions at $\sqrt{s_{NN}} = 5.02 \text{ TeV}$ are simultaneously explained by the coalescence model. Our extracted results for $R_f(p_T)$ can provide quantitative references for future measurements of HBT interferometry radius from two-nucleon correlations. Through light nucleus production, we provide an alternative way to the HBT interferometry radius of the hadronic source system.

351

B. The p_T spectra of light nuclei

352 The p_T spectra of primordial nucleons are necessary inputs for computing p_T distributions of light nuclei in the co-353 alescence model. We here use the blast-wave model to get 354 p_T distribution functions of primordial protons by fitting the 355 experimental data of prompt (anti)protons in Ref. [80]. The 356 blast-wave function [81] is given as

357

$$\frac{d^2N}{2\pi p_T dp_T dy} \propto \int_0^R r dr m_T I_0 \left(\frac{p_T \sinh \rho}{T_{kin}} \right) K_1 \left(\frac{m_T \cosh \rho}{T_{kin}} \right), \quad (33)$$

358

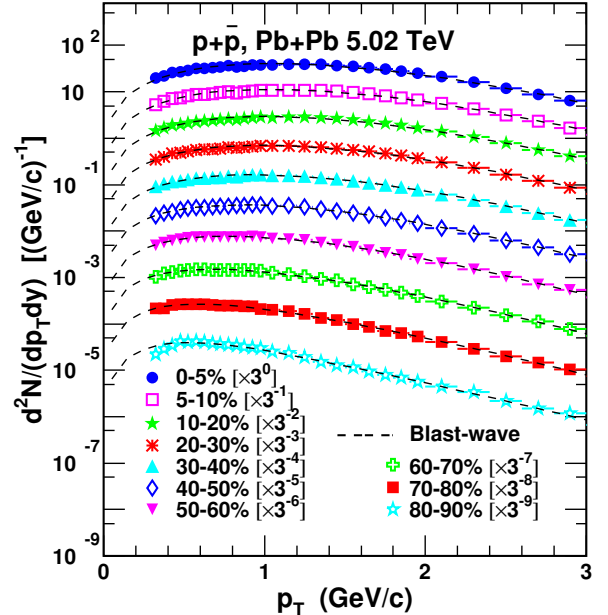
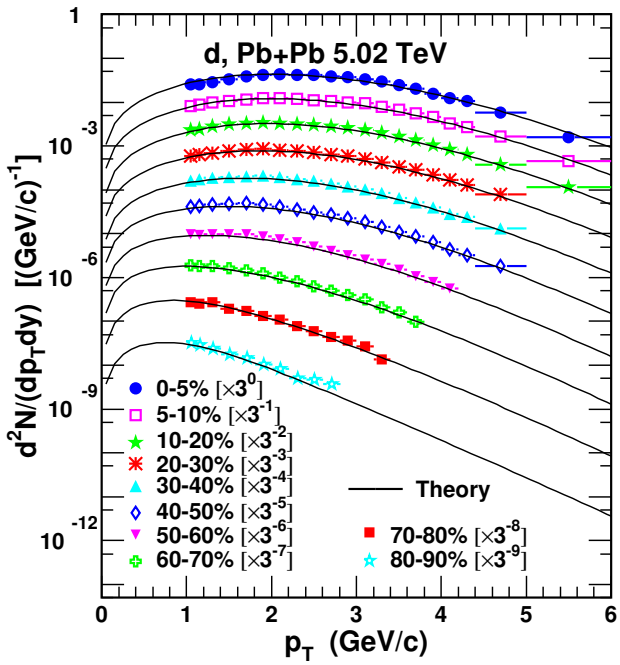


Fig. 3. The p_T spectra of prompt protons plus antiprotons in different centralities in Pb+Pb collisions at $\sqrt{s_{NN}} = 5.02 \text{ TeV}$. Symbols with error bars are experimental data [80] and dashed lines are results of the blast-wave model.

360 where r is the radial distance in the transverse plane and R is 361 the fireball radius. I_0 and K_1 are the modified Bessel functions, and the velocity profile $\rho = \tanh^{-1}[\beta_s(\frac{r}{R})^n]$. The 362

363 surface velocity β_s , the kinetic freeze-out temperature T_{kin}
 364 and n are fitting parameters.

365 Fig. 3 shows the p_T spectra of prompt protons plus antipro-
 366 tons in different centralities in Pb+Pb collisions at $\sqrt{s_{NN}} =$
 367 5.02 TeV. Symbols with error bars are experimental data [80],
 368 and dashed lines are the results of the blast-wave model. The
 369 p_T spectra in different centralities are scaled by different fac-
 370 tors for clarity as shown in the figure. For the primordial neu-
 371 tron p_T spectra, we adopt the same as those of primordial
 372 protons as we focus on light nucleus production at midrapidity
 373 at so high LHC energy that the isospin symmetry is well
 374 satisfied.



407 Fig. 4. The p_T spectra of deuterons in different centralities in Pb+Pb
 408 collisions at $\sqrt{s_{NN}} = 5.02$ TeV. Symbols with error bars are exper-
 409 imental data [77] and solid lines are theoretical results.

410 We first calculate the p_T spectra of deuterons in Pb+Pb col-
 411 lisions at $\sqrt{s_{NN}} = 5.02$ TeV in 0 – 5%, 5 – 10%, 10 – 20%,
 412 20 – 30%, 30 – 40%, 40 – 50%, 50 – 60%, 60 – 70%, 70 – 80%
 413 and 80 – 90% centralities. Different solid lines scaled by dif-
 414 ferent factors for clarity in Fig. 4 are our theoretical results.
 415 Symbols with error bars are experimental data from the AL-
 416 ICE collaboration [30]. We then compute the p_T spectra of
 417 ^3He and \bar{t} in Pb+Pb collisions at $\sqrt{s_{NN}} = 5.02$ TeV in dif-
 418 ferent centralities. Different solid lines in Fig. 5 are our theo-
 419 retical results, which agree with the available data denoted by
 420 filled symbols [30]. From Fig. 4 and Fig. 5, one can see the
 421 nucleon coalescence is the dominant mechanism for light nu-
 422 cleus production in Pb+Pb collisions at $\sqrt{s_{NN}} = 5.02$ TeV.
 423 More precise measurements for ^3He and \bar{t} in wide p_T range
 424 in the forthcoming future can help further test the coalescence
 425 mechanism, especially in peripheral Pb+Pb collisions.

391 **C. Averaged transverse momenta and yield rapidity densities
 392 of light nuclei**

393 We here study the averaged transverse momenta $\langle p_T \rangle$ and
 394 yield rapidity densities dN/dy of d , ^3He and \bar{t} . Our theo-
 395 retical results are in the fourth and sixth columns in Table
 396 1. Experimental data in the third and fifth columns are from
 397 Refs. [30, 77]. A decreasing trend for both $\langle p_T \rangle$ and dN/dy
 398 from central to peripheral collisions is observed. This is be-
 399 cause in more central collisions more energy is deposited in
 400 the midrapidity region and collective evolution exists longer.
 401 Theoretical results for d , ^3He and \bar{t} are consistent with the
 402 corresponding data within the experimental uncertainties ex-
 403 cept for a very little underestimation for the dN/dy of \bar{t} in a
 404 peripheral 50-90% collision. Such underestimation needs to
 405 be confirmed by future precise data.

406 **D. Yield ratios of light nuclei**

407 Yield ratios of light nuclei carry information on intrinsic
 408 production correlations of different light nuclei and are pre-
 409 dicted to have nontrivial behaviors [67]. In this subsection,
 410 we study the centrality dependence of different yield ratios,
 411 such as d/p , $^3\text{He}/\bar{p}$, d/p^2 , $^3\text{He}/\bar{p}^3$ and $\bar{t}/^3\text{He}$.

412 Fig. 6 (a) and (b) show the $dN_{ch}/d\eta$ dependence of d/p
 413 and $^3\text{He}/\bar{p}$ in Pb+Pb collisions at $\sqrt{s_{NN}} = 5.02$ TeV. Filled
 414 circles with error bars are experimental data [82], and open
 415 circles connected with dashed lines to guide the eye are the-
 416 oretical results. From Eq. (15) we approximately have the
 417 p_T -integrated yield ratio

$$418 \frac{d}{p} \propto \frac{N_p}{\langle R_f \rangle^3 \left(C_0 + \frac{\sigma_d^2}{\langle R_f \rangle^2} \right) \sqrt{\frac{C_0}{\langle \gamma \rangle^2} + \frac{\sigma_d^2}{\langle R_f \rangle^2}}} \\ 419 = \frac{N_p}{\langle R_f \rangle^3 / \langle \gamma \rangle} \times \frac{1}{\left(C_0 + \frac{\sigma_d^2}{\langle R_f \rangle^2} \right) \sqrt{C_0 + \frac{\sigma_d^2}{\langle R_f \rangle^2 / \langle \gamma \rangle^2}}}, \quad (34)$$

420 where angle brackets denote the averaged values. Eq. (34)
 421 gives that the behavior of d/p is determined by two factors.
 422 One is the nucleon number density $\frac{N_p}{\langle R_f \rangle^3 / \langle \gamma \rangle}$ and the other
 423 is the suppression effect from the relative size of the d to the
 424 hadronic source system $\frac{\sigma_d}{\langle R_f \rangle}$. Similar case holds for $^3\text{He}/\bar{p}$.
 425 The nucleon number density decreases especially from semi-
 426 central to central collisions [80], which makes d/p and $^3\text{He}/\bar{p}$
 427 decrease with the increasing $dN_{ch}/d\eta$. The relative size $\frac{\sigma_d}{\langle R_f \rangle}$
 428 decreases and its suppression effect becomes weak in large
 429 hadronic systems, which makes d/p and $^3\text{He}/\bar{p}$ increase with
 430 the increasing $dN_{ch}/d\eta$ [83]. For very high $dN_{ch}/d\eta$ area,
 431 the difference of the suppression extents in different centrali-
 432 ties becomes insignificant and the decreasing nucleon number
 433 density dominates the decreasing behavior of d/p and $^3\text{He}/\bar{p}$.
 434 For low $dN_{ch}/d\eta$ area, different suppression extents of the
 435 relative size in different centralities make d/p and $^3\text{He}/\bar{p}$ in-
 436 crease as a function of $dN_{ch}/d\eta$. The final conjunct result
 437 from the nucleon number density and the suppression effect

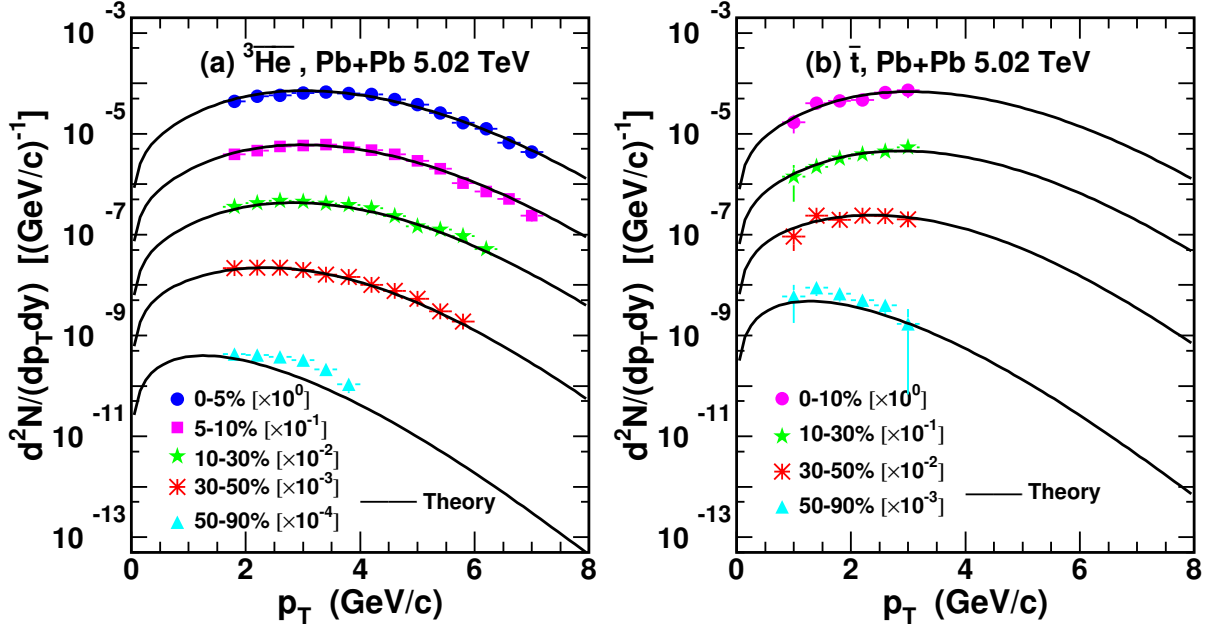


Fig. 5. The p_T spectra of (a) ${}^3\bar{\text{He}}$ and (b) \bar{t} in different centralities in Pb+Pb collisions at $\sqrt{s_{NN}} = 5.02$ TeV. Filled symbols with error bars are experimental data [30] and solid lines are theoretical results.

Table 1. Averaged transverse momenta $\langle p_T \rangle$ and yield rapidity densities dN/dy of d , ${}^3\bar{\text{He}}$ and \bar{t} in different centralities in Pb+Pb collisions at $\sqrt{s_{NN}} = 5.02$ TeV. Experimental data in the third and fifth columns are from Refs. [30, 77]. Theoretical results are in the fourth and sixth columns.

Centrality	$\langle p_T \rangle$ (GeV/c)		dN/dy	
	Data	Theory	Data	Theory
0 – 5%	$2.45 \pm 0.00 \pm 0.09$	2.37	$(1.19 \pm 0.00 \pm 0.21) \times 10^{-1}$	1.22×10^{-1}
5 – 10%	$2.41 \pm 0.01 \pm 0.10$	2.33	$(1.04 \pm 0.00 \pm 0.19) \times 10^{-1}$	1.01×10^{-1}
10 – 20%	$2.34 \pm 0.00 \pm 0.11$	2.28	$(8.42 \pm 0.02 \pm 1.50) \times 10^{-2}$	7.86×10^{-2}
20 – 30%	$2.21 \pm 0.00 \pm 0.12$	2.18	$(6.16 \pm 0.02 \pm 1.10) \times 10^{-2}$	5.58×10^{-2}
d	30 – 40%	$2.05 \pm 0.00 \pm 0.12$	2.04	$(4.25 \pm 0.01 \pm 0.75) \times 10^{-2}$
	40 – 50%	$1.88 \pm 0.01 \pm 0.12$	1.87	$(2.73 \pm 0.01 \pm 0.48) \times 10^{-2}$
	50 – 60%	$1.70 \pm 0.01 \pm 0.11$	1.66	$(1.62 \pm 0.01 \pm 0.28) \times 10^{-2}$
	60 – 70%	$1.46 \pm 0.01 \pm 0.12$	1.45	$(8.35 \pm 0.14 \pm 1.43) \times 10^{-3}$
	70 – 80%	$1.27 \pm 0.02 \pm 0.11$	1.25	$(3.52 \pm 0.06 \pm 0.63) \times 10^{-3}$
	80 – 90%	$1.09 \pm 0.02 \pm 0.40$	1.10	$(1.13 \pm 0.03 \pm 0.23) \times 10^{-3}$
	0 – 5%	$3.465 \pm 0.013 \pm 0.154 \pm 0.144$	3.26	$(24.70 \pm 0.28 \pm 2.29 \pm 0.30) \times 10^{-5}$
	5 – 10%	$3.368 \pm 0.014 \pm 0.141 \pm 0.132$	3.21	$(20.87 \pm 0.26 \pm 1.95 \pm 0.43) \times 10^{-5}$
	10 – 30%	$3.237 \pm 0.021 \pm 0.157 \pm 0.150$	3.08	$(15.94 \pm 0.31 \pm 1.53 \pm 0.34) \times 10^{-5}$
	30 – 50%	$2.658 \pm 0.016 \pm 0.084 \pm 0.049$	2.64	$(7.56 \pm 0.13 \pm 0.70 \pm 0.10) \times 10^{-5}$
${}^3\bar{\text{He}}$	50 – 90%	$2.057 \pm 0.023 \pm 0.090 \pm 0.027$	1.77	$(1.19 \pm 0.08 \pm 0.16 \pm 0.14) \times 10^{-5}$
	0 – 10%	$3.368 \pm 0.241 \pm 0.060$	3.27	$(24.45 \pm 1.75 \pm 2.71) \times 10^{-5}$
	10 – 30%	$3.015 \pm 0.286 \pm 0.040$	3.11	$(14.19 \pm 1.35 \pm 1.29) \times 10^{-5}$
	30 – 50%	$2.524 \pm 0.593 \pm 0.180$	2.68	$(7.24 \pm 1.70 \pm 0.65) \times 10^{-5}$
	50 – 90%	$1.636 \pm 0.226 \pm 0.040$	1.80	$(1.66 \pm 0.23 \pm 0.16) \times 10^{-5}$
\bar{t}	0 – 10%	$3.368 \pm 0.241 \pm 0.060$	3.27	$(24.45 \pm 1.75 \pm 2.71) \times 10^{-5}$
	10 – 30%	$3.015 \pm 0.286 \pm 0.040$	3.11	$(14.19 \pm 1.35 \pm 1.29) \times 10^{-5}$
	30 – 50%	$2.524 \pm 0.593 \pm 0.180$	2.68	$(7.24 \pm 1.70 \pm 0.65) \times 10^{-5}$
	50 – 90%	$1.636 \pm 0.226 \pm 0.040$	1.80	$(1.66 \pm 0.23 \pm 0.16) \times 10^{-5}$

438 makes d/p and ${}^3\bar{\text{He}}/\bar{p}$ first increase from peripheral to semi-
439 central collisions and then decrease from semi-central to cen-
440 tral collisions, just as shown in Fig. 6 (a) and (b).

441 Fig. 6 (c) and (d) show d/p^2 and ${}^3\bar{\text{He}}/\bar{p}^3$ as a function of
442 $dN_{ch}/d\eta$ in Pb+Pb collisions at $\sqrt{s_{NN}} = 5.02$ TeV. Filled
443 circles with error bars are experimental data [82]. Open cir-
444 cles connected with dashed lines to guide the eye are theoret-

445 ical results. Both of them give explicit decreasing trends with
446 the increasing $dN_{ch}/d\eta$, which are very different from the
447 previous d/p and ${}^3\bar{\text{He}}/\bar{p}$. Recalling that d/p^2 and ${}^3\bar{\text{He}}/\bar{p}^3$
448 represent the probability of any pn -pair coalescing into a
449 deuteron and that of any $\bar{p}\bar{p}n$ -cluster coalescing into a ${}^3\bar{\text{He}}$.
450 This means that it is more difficult for any pn -pair or $\bar{p}\bar{p}n$ -
451 cluster to recombine into a deuteron or ${}^3\bar{\text{He}}$ in the larger

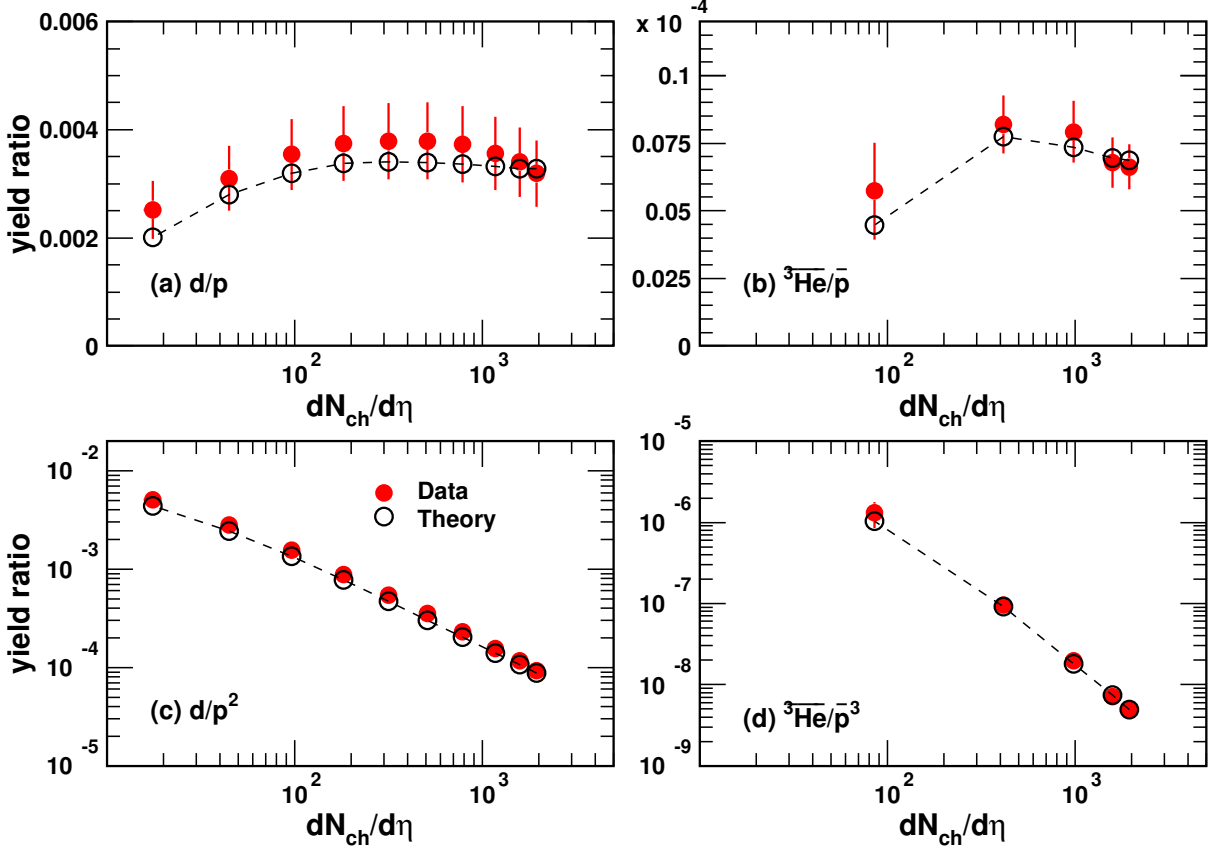


Fig. 6. Yield ratios (a) d/p , (b) ${}^3\text{He}/\bar{p}$, (c) d/p^2 and (d) ${}^3\text{He}/\bar{p}^3$ as a function of $dN_{ch}/d\eta$ in Pb+Pb collisions at $\sqrt{s_{NN}} = 5.02$ TeV. Filled circles with error bars are experimental data [30, 77] and open circles connected with dashed lines to guide the eye are theoretical results.

452 hadronic system produced in a more central collision.

453 The yield ratio $t/{}^3\text{He}$ is proposed as a valuable probe to
 454 distinguish the thermal production and the coalescence pro-
 455 duction for light nuclei [67]. In the coalescence picture, it is
 456 always larger than one and approaches one at large R_f where
 457 the suppression effect from the nucleus size can be ignored.
 458 The smaller R_f , the higher deviation of $t/{}^3\text{He}$ from one. The
 459 same case holds for $\bar{t}/{}^3\text{He}$. Fig. 7 shows $\bar{t}/{}^3\text{He}$ as a function
 460 of p_T in Pb+Pb collisions at $\sqrt{s_{NN}} = 5.02$ TeV in different
 461 centralities 0-10%, 10-30%, 30-50% and 50-90%. Filled cir-
 462 cles with error bars are experimental data [30] and solid lines
 463 are theoretical results. The reference line of one is plotted
 464 with dotted lines. With the increasing p_T , R_f decreases, so
 465 our theoretical results increase. This feature is very different
 466 from that in the thermal model, where the expectation for this
 467 ratio is one [47]. The trend of the data in 0-10%, 10-30%,
 468 and 30-50% centralities indicates an increasing hint but a fi-
 469 nal conclusion is hard to make due to the limited p_T range and
 470 the large error bars. Data in the peripheral 50-90% centrality
 471 seems to decrease, but further more precise measurements are
 472 needed to confirm. More precise data in the near future can
 473 be used to further distinguish production mechanisms of ${}^3\text{He}$
 474 and \bar{t} .

475 The p_T -integrated yield ratio $\bar{t}/{}^3\text{He}$ as a function of
 476 $dN_{ch}/d\eta$ is in Fig. 8. Filled circles with error bars are exper-

477 imental data [30] and open circles connected with the dashed
 478 line to guide the eye are theoretical results. The reference line
 479 of one is also plotted with the dotted line. $\bar{t}/{}^3\text{He}$ exhibits a
 480 decreasing trend. This is because larger $dN_{ch}/d\eta$, i.e., larger
 481 R_f , makes $\bar{t}/{}^3\text{He}$ decrease closer to one. Theoretical results
 482 of $\bar{t}/{}^3\text{He}$ in the coalescence model give non-flat behaviors as
 483 a function of $dN_{ch}/d\eta$. This is due to different relative pro-
 484 duction suppression between ${}^3\text{He}$ and \bar{t} from their own sizes
 485 at different hadronic system scales.

IV. RESULTS OF THE HYPERTRITON AND Ω -HYPERNUCLEI

488 In this section, we use the coalescence model in Sec. II
 489 to study productions of the hypertriton and Ω -hypernuclei.
 490 We give the results of the p_T spectra, the averaged p_T , and
 491 yield rapidity densities of the ${}^3\text{H}$. We present the predictions
 492 of different Ω -hypernuclei, such as $H(p\Omega^-)$, $H(n\Omega^-)$ and
 493 $H(pn\Omega^-)$. We propose two groups of observables, both of
 494 which exhibit novel behaviors. One group refers to the aver-
 495 aged p_T ratios of the light (hyper-)nuclei to the protons (hy-
 496 perons), and the other the centrality-dependent yield ratios of
 497 theirs.

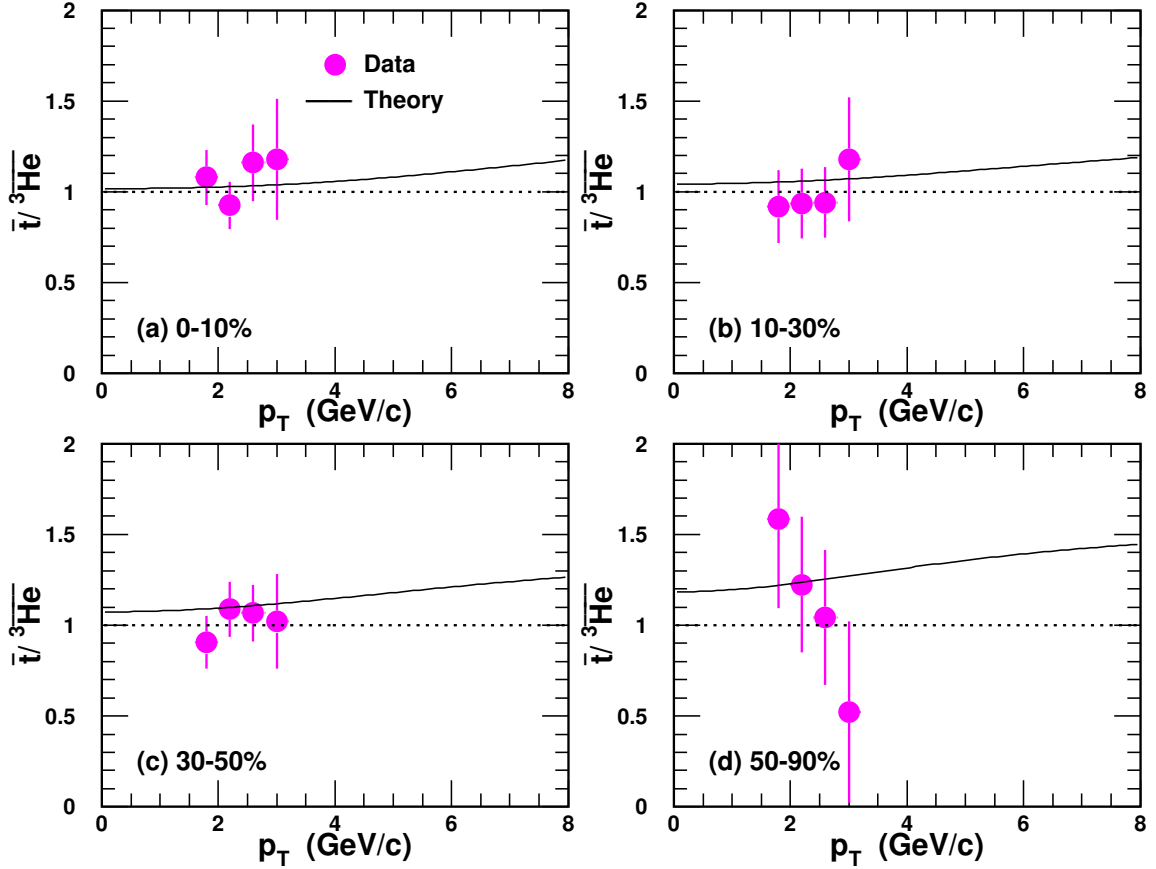


Fig. 7. Yield ratio $\bar{t}/\bar{^3\text{He}}$ as a function of p_T in different centralities in Pb+Pb collisions at $\sqrt{s_{NN}} = 5.02$ TeV. Filled circles with error bars are experimental data [30] and solid lines are theoretical results.

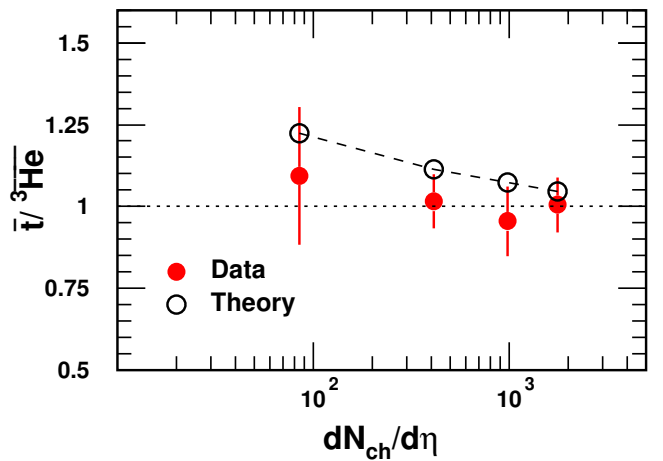


Fig. 8. Yield ratio $\bar{t}/\bar{^3\text{He}}$ as a function of $dN_{ch}/d\eta$ in Pb+Pb collisions at $\sqrt{s_{NN}} = 5.02$ TeV. Filled circles with error bars are experimental data [30] and open circles connected with dashed lines to guide the eye are theoretical results.

498 A. The p_T spectra of Λ and Ω^- hyperons

499 The p_T spectra of Λ and Ω^- hyperons are necessary for
500 computing p_T distributions of ^3H and Ω -hypernuclei. We
501 use the blast-wave model to get p_T distribution functions by
502 fitting the experimental data of Λ and Ω^- in Pb+Pb collisions
503 at $\sqrt{s_{NN}} = 5.02$ TeV in 0 – 10%, 10 – 30%, and 30 – 50%
504 centralities [84]. They are shown in Fig. 9. Filled symbols
505 with error bars are experimental data [84], and dashed lines
506 are the results of the blast-wave model. The p_T spectra in
507 0 – 10%, 10 – 30% and 30 – 50% centralities are scaled by 2^0 ,
508 2^{-1} and 2^{-2} , respectively, for clarity in the figure. We have
509 also studied the p_T spectra of Λ and Ω^- hyperons with the
510 Quark Combination Model developed by the Shandong group
511 (SDQCM) in another work [85], where the results are consis-
512 tent with the blast-wave model at low and intermediate p_T
513 regions. We in the following use these Λ and Ω^- hyperons in
514 Fig. 9 to compute productions of the ^3H and Ω -hypernuclei.
515 The values of parameters a and b in $R_f(p_T)$ for $H(p\Omega^-)$ and
516 $H(n\Omega^-)$ are the same as the deuteron, and those for ^3H and
517 $H(pn\Omega^-)$ are the same with ^3He . So our calculated results
518 for the ^3H and Ω -hypernuclei are parameter-free, and they
519 are more potent for further testing of the coalescence mecha-
520 nism in describing the productions of nuclei with strangeness

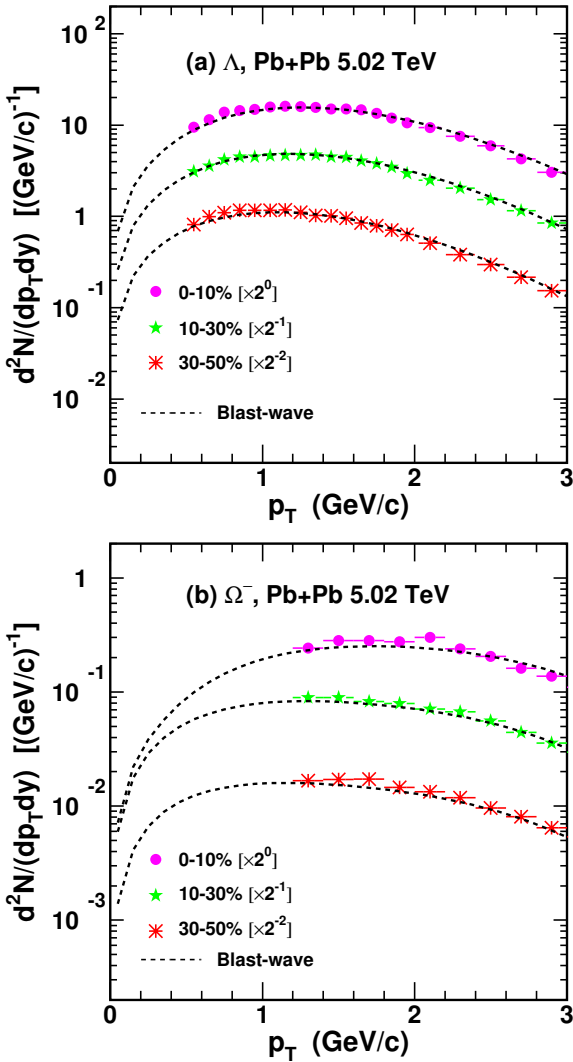


Fig. 9. The p_T spectra of (a) Λ and (b) Ω^- in different centralities in Pb+Pb collisions at $\sqrt{s_{NN}} = 5.02$ TeV. Symbols with error bars are experimental data [84] and dashed lines are the results of the blast-wave model.

521 flavor quantum number.

B. The results of the $^3\Lambda$ H

523 Based on Eq. (27), we compute the production of the $^3\Lambda$ H. 524 Considering that the experimental measurements of the $^3\Lambda$ H 525 suggest a halo structure with a d core encircled by a Λ , we first 526 use $\sigma_1 = \sqrt{\frac{2(m_p+m_n)^2}{3(m_p^2+m_n^2)} R_d}$ and $\sigma_2 = \sqrt{\frac{2(m_d+m_\Lambda)^2}{9(m_d^2+m_\Lambda^2)} r_{\Lambda d}}$. The 527 $\Lambda-d$ distance $r_{\Lambda d}$ is evaluated via $r_{\Lambda d} = \sqrt{\hbar^2/(4\mu B_\Lambda)}$ [86], 528 where μ is the reduced mass and the binding energy B_Λ 529 here is adopted to be the latest and most precise mea- 530 surement to date 102 KeV [33]. We also take a spherical 531 shape for the $^3\Lambda$ H to execute the calculation to study the 532 influence of the shape on its production. In this case, $\sigma_1 =$

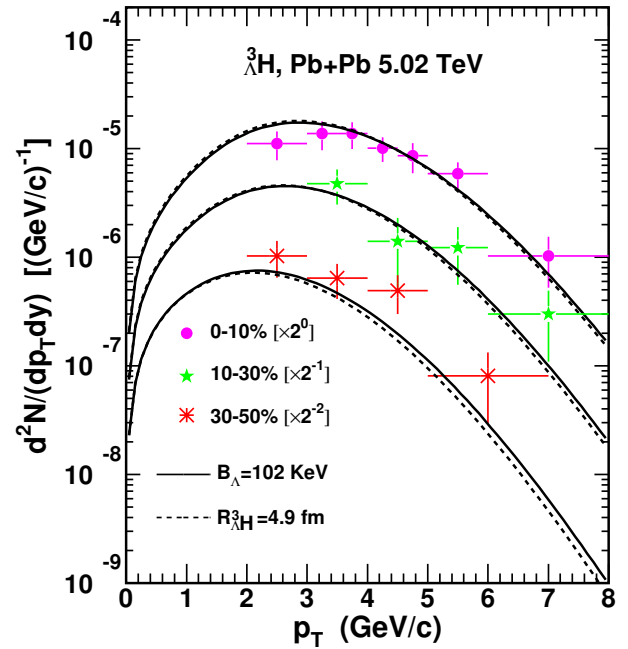


Fig. 10. The p_T spectra of the $^3\Lambda$ H in different centralities in Pb+Pb collisions at $\sqrt{s_{NN}} = 5.02$ TeV. Filled symbols with error bars are the experimental data [68]. The solid and dashed lines are the theoretical results with a halo structure and a spherical shape, respectively.

$$\begin{aligned}
 & 533 \sqrt{\frac{m_\Lambda(m_p+m_n)(m_p+m_n+m_\Lambda)}{m_p m_n(m_p+m_n)+m_n m_\Lambda(m_n+m_\Lambda)+m_\Lambda m_p(m_\Lambda+m_p)}} R_{^3\Lambda H}, \quad \sigma_2 \\
 & 534 = \sqrt{\frac{4m_p m_n(m_p+m_n+m_\Lambda)^2}{3(m_p+m_n)[m_p m_n(m_p+m_n)+m_n m_\Lambda(m_n+m_\Lambda)+m_\Lambda m_p(m_\Lambda+m_p)]}} R_{^3\Lambda H}, \\
 & 535 \text{ where the root-mean-square radius } R_{^3\Lambda H} \text{ is adopted to be } 4.9 \\
 & 536 \text{ fm [18]. Fig. 10 shows the } p_T \text{ spectra of the } ^3\Lambda H \text{ in } 0-10\%, \\
 & 537 10-30\%, \text{ and } 30-50\% \text{ centralities in Pb+Pb collisions at} \\
 & 538 \sqrt{s_{NN}} = 5.02 \text{ TeV. Filled symbols with error bars are the} \\
 & 539 \text{ experimental data [68]. The solid lines are the theoretical} \\
 & 540 \text{ results of the coalescence model with a halo structure and the} \\
 & 541 \text{ dashed lines are those for a spherical shape. The } p_T \text{ spectra} \\
 & 542 \text{ in different centralities are scaled by different factors for} \\
 & 543 \text{ clarity as shown in the figure. From Fig. 10, one can see that} \\
 & 544 \text{ there exists a weak difference in the theoretical results of the} \\
 & 545 p_T \text{ spectra between a halo structure and a spherical shape,} \\
 & 546 \text{ and the latter gives a little softer } p_T \text{ spectra. The results} \\
 & 547 \text{ with a halo structure approach to the available data better,} \\
 & 548 \text{ for both amplitude and shape. This point can also be seen} \\
 & 549 \text{ in the averaged transverse momenta } \langle p_T \rangle \text{ and yield rapidity} \\
 & 550 \text{ densities } dN/dy \text{ of } ^3\Lambda H \text{ hereunder.}
 \end{aligned}$$

551 Table 2 presents the averaged transverse momenta $\langle p_T \rangle$ 552 and yield rapidity densities dN/dy of $^3\Lambda$ H in different centralities 553 in Pb+Pb collisions at $\sqrt{s_{NN}} = 5.02$ TeV. Experimental data 554 in the seventh column are from Ref. [68]. Theory-4.9 in the 555 third and eighth columns denotes theoretical results with a 556 spherical shape at $R_{^3\Lambda H} = 4.9$ fm. Theory-102 in the fourth 557 and ninth columns are theoretical results at $B_\Lambda = 102$ keV. 558 Theory-148 in the fifth and tenth columns are theoretical re- 559 sults at a word averaged value of $B_\Lambda = 148$ keV [33]. We 560 also give theoretical results at $B_\Lambda = 410$ keV measured by the

Table 2. Averaged transverse momenta $\langle p_T \rangle$ and yield rapidity densities dN/dy of $^3\Lambda\text{H}$ in different centralities in Pb+Pb collisions at $\sqrt{s_{NN}} = 5.02$ TeV. Experimental data in the seventh column are from Ref. [68]. Theory-4.9 denotes theoretical results with a spherical shape at $R_{^3\Lambda\text{H}} = 4.9$ fm. Theory-102, Theory-148 and Theory-410 denote theoretical results with a halo structure at $B_\Lambda = 102, 148$ and 410 KeV, respectively.

Centrality	$\langle p_T \rangle$ (GeV/c)				dN/dy ($\times 10^{-9}$)				
	Theory-4.9	Theory-102	Theory-148	Theory-410	Data	Theory-4.9	Theory-102	Theory-148	Theory-410
$^3\Lambda\text{H}$	0 – 10%	3.16	3.19	3.24	3.37	$4.83 \pm 0.23 \pm 0.57$	6.09	5.96	7.75
	10 – 30%	2.90	2.94	2.99	3.11	$2.62 \pm 0.25 \pm 0.40$	2.98	2.99	4.07
	30 – 50%	2.46	2.52	2.55	2.65	$1.27 \pm 0.10 \pm 0.14$	0.875	0.932	1.35

561 STAR collaboration [31] in the sixth and eleventh columns. 561 STAR collaboration [31] in the sixth and eleventh columns.
 562 Clear decreasing trends for $\langle p_T \rangle$ and dN/dy from central to 562 Clear decreasing trends for $\langle p_T \rangle$ and dN/dy from central to
 563 semi-central collisions are observed. This is the same as light 563 semi-central collisions are observed. This is the same as light
 564 nuclei, which is due to that in more central collisions more en- 564 nuclei, which is due to that in more central collisions more en-
 565 ergy is deposited in the midrapidity region and collective evo- 565 ergy is deposited in the midrapidity region and collective evo-
 566 lution exists longer. For the halo structure, with the increase 566 lution exists longer. For the halo structure, with the increase
 567 of the B_Λ , the size of the $^3\Lambda\text{H}$ decreases, and the suppression 567 of the B_Λ , the size of the $^3\Lambda\text{H}$ decreases, and the suppression
 568 effect from the $^3\Lambda\text{H}$ size becomes relatively weak. This leads 568 effect from the $^3\Lambda\text{H}$ size becomes relatively weak. This leads
 569 to an increase of dN/dy with the increasing B_Λ . Besides 569 to an increase of dN/dy with the increasing B_Λ . Besides
 570 dN/dy , such production suppression effect also affects the 570 dN/dy , such production suppression effect also affects the
 571 p_T distribution [67, 87]. This is because the suppression ef- 571 p_T distribution [67, 87]. This is because the suppression ef-
 572 fect becomes stronger with a larger nucleus size in a smaller 572 fect becomes stronger with a larger nucleus size in a smaller
 573 system. Recalling that $R_f(p_T)$ decreases with p_T , the $^3\Lambda\text{H}$ 573 system. Recalling that $R_f(p_T)$ decreases with p_T , the $^3\Lambda\text{H}$
 574 production is more suppressed in larger p_T areas in the case 574 production is more suppressed in larger p_T areas in the case
 575 of larger $^3\Lambda\text{H}$ size. So there exists a decreasing trend for $\langle p_T \rangle$ 575 of larger $^3\Lambda\text{H}$ size. So there exists a decreasing trend for $\langle p_T \rangle$
 576 with the decreasing B_Λ , as shown in Table 2. This is the rea- 576 with the decreasing B_Λ , as shown in Table 2. This is the rea-
 577 son why the $\langle p_T \rangle$ of $^3\Lambda\text{H}$ is even smaller than that of the triton 577 son why the $\langle p_T \rangle$ of $^3\Lambda\text{H}$ is even smaller than that of the triton
 578 while the $\langle p_T \rangle$ of Λ is larger than the nucleon. 578 while the $\langle p_T \rangle$ of Λ is larger than the nucleon.

C. Predictions of Ω -hypernuclei

580 The nucleon- Ω dibaryon in the S-wave and spin-2 chan- 580 The nucleon- Ω dibaryon in the S-wave and spin-2 chan-
 581 nel is an interesting candidate for the deuteron-like state [88, 581 nel is an interesting candidate for the deuteron-like state [88,
 582 89]. The HAL QCD collaboration has reported the root- 582 89]. The HAL QCD collaboration has reported the root-
 583 mean-square radius of $H(p\Omega^-)$ is about 3.24 fm and that 583 mean-square radius of $H(p\Omega^-)$ is about 3.24 fm and that
 584 of $H(n\Omega^-)$ is 3.77 fm [90]. According to Eq. (15), we 584 of $H(n\Omega^-)$ is 3.77 fm [90]. According to Eq. (15), we
 585 study their productions, where the spin degeneracy factor 585 study their productions, where the spin degeneracy factor
 586 $g_{H(p\Omega^-)} = g_{H(n\Omega^-)} = 5/8$. Fig. 11 shows predictions for 586 $g_{H(p\Omega^-)} = g_{H(n\Omega^-)} = 5/8$. Fig. 11 shows predictions for
 587 their p_T spectra in 0 – 10%, 10 – 30%, and 30 – 50% central- 587 their p_T spectra in 0 – 10%, 10 – 30%, and 30 – 50% central-
 588 ities with solid, dashed, and dash-dotted lines, respectively, 588 ities with solid, dashed, and dash-dotted lines, respectively,
 589 in Pb+Pb collisions at $\sqrt{s_{NN}} = 5.02$ TeV. Different lines are 589 in Pb+Pb collisions at $\sqrt{s_{NN}} = 5.02$ TeV. Different lines are
 590 scaled by different factors for clarity as shown in the figure. 590 scaled by different factors for clarity as shown in the figure.

Table 3. Predictions of averaged transverse momenta $\langle p_T \rangle$ and yield rapidity densities dN/dy of $H(p\Omega^-)$ and $H(n\Omega^-)$ in different centralities in Pb+Pb collisions at $\sqrt{s_{NN}} = 5.02$ TeV.

Centrality	$\langle p_T \rangle$ (GeV/c)	dN/dy ($\times 10^{-4}$)
$H(p\Omega^-)$	0 – 10%	2.84
	10 – 30%	2.44
	30 – 50%	2.18
$H(n\Omega^-)$	0 – 10%	2.81
	10 – 30%	2.41
	30 – 50%	2.15

591 Table 3 presents predictions of the averaged transverse mo- 591 Table 3 presents predictions of the averaged transverse mo-
 592 ments $\langle p_T \rangle$ and yield rapidity densities dN/dy of $H(p\Omega^-)$ 592 ments $\langle p_T \rangle$ and yield rapidity densities dN/dy of $H(p\Omega^-)$
 593 and $H(n\Omega^-)$. Both of them decrease from central to semi- 593 and $H(n\Omega^-)$. Both of them decrease from central to semi-
 594 central collisions, similar to light nuclei and the $^3\Lambda\text{H}$. The 594 central collisions, similar to light nuclei and the $^3\Lambda\text{H}$. The
 595 slightly lower results of $H(n\Omega^-)$ than $H(p\Omega^-)$ come from 595 slightly lower results of $H(n\Omega^-)$ than $H(p\Omega^-)$ come from
 596 its slightly larger size.

597 The $H(pn\Omega^-)$ with maximal spin- $\frac{5}{2}$ is proposed to be one 597 The $H(pn\Omega^-)$ with maximal spin- $\frac{5}{2}$ is proposed to be one
 598 of the most promising partners of the t and $^3\Lambda\text{H}$ with multi- 598 of the most promising partners of the t and $^3\Lambda\text{H}$ with multi-
 599 strangeness flavor quantum number [91]. With Eq. (27), 599 strangeness flavor quantum number [91]. With Eq. (27),
 600 we study its production and the spin degeneracy factor 600 we study its production and the spin degeneracy factor
 601 $g_{H(pn\Omega^-)} = 3/8$. As its root-mean-square radius $R_{H(pn\Omega^-)}$ 601 $g_{H(pn\Omega^-)} = 3/8$. As its root-mean-square radius $R_{H(pn\Omega^-)}$
 602 is undetermined, we adopt 1.5, 2.0, and 2.5 fm to execute cal- 602 is undetermined, we adopt 1.5, 2.0, and 2.5 fm to execute cal-
 603 culations, respectively. Fig. 12 shows predictions of the p_T 603 culations, respectively. Fig. 12 shows predictions of the p_T
 604 spectra in 0 – 10%, 10 – 30% and 30 – 50% centralities in 604 spectra in 0 – 10%, 10 – 30% and 30 – 50% centralities in
 605 Pb+Pb collisions at $\sqrt{s_{NN}} = 5.02$ TeV. Solid, dashed, and 605 Pb+Pb collisions at $\sqrt{s_{NN}} = 5.02$ TeV. Solid, dashed, and
 606 dash-dotted lines denote results with $R_{H(pn\Omega^-)} = 1.5, 2.0,$ 606 dash-dotted lines denote results with $R_{H(pn\Omega^-)} = 1.5, 2.0,$
 607 and 2.5 fm, respectively, which are scaled by different factors 607 and 2.5 fm, respectively, which are scaled by different factors
 608 for clarity as shown in the figure. Table 4 presents predictions 608 for clarity as shown in the figure. Table 4 presents predictions
 609 of the averaged transverse momenta $\langle p_T \rangle$ and yield rapidity 609 of the averaged transverse momenta $\langle p_T \rangle$ and yield rapidity
 610 densities dN/dy of $H(pn\Omega^-)$. Theory-1.5, Theory-2.0, and 610 densities dN/dy of $H(pn\Omega^-)$. Theory-1.5, Theory-2.0, and
 611 Theory-2.5 denote theoretical results at $R_{H(pn\Omega^-)} = 1.5, 2.0,$ 611 Theory-2.5 denote theoretical results at $R_{H(pn\Omega^-)} = 1.5, 2.0,$
 612 and 2.5 fm, respectively. 612 and 2.5 fm, respectively.

613 Our predictions in central collisions for $H(p\Omega^-)$ and 613 Our predictions in central collisions for $H(p\Omega^-)$ and
 614 $H(n\Omega^-)$ are in the same magnitudes with BLWC and 614 $H(n\Omega^-)$ are in the same magnitudes with BLWC and
 615 AMPTC models in Ref. [92], and those for $H(pn\Omega^-)$ are in 615 AMPTC models in Ref. [92], and those for $H(pn\Omega^-)$ are in
 616 the same magnitude as in Ref. [93]. Our predictions in other 616 the same magnitude as in Ref. [93]. Our predictions in other
 617 centralities provide more detailed references for centrality- 617 centralities provide more detailed references for centrality-
 618 dependent measurements of these Ω -hypernuclei in future 618 dependent measurements of these Ω -hypernuclei in future
 619 LHC experiments.

D. Averaged transverse momentum ratios and yield ratios

621 Based on the results of light nuclei and hypernuclei above, 621 Based on the results of light nuclei and hypernuclei above,
 622 we study two groups of interesting observables as powerful 622 we study two groups of interesting observables as powerful
 623 probes for the production correlations of different species of 623 probes for the production correlations of different species of
 624 nuclei. One group refers to the $\langle p_T \rangle$ ratios of light nuclei 624 nuclei. One group refers to the $\langle p_T \rangle$ ratios of light nuclei
 625 to protons and hypernuclei to hyperons. The other is their 625 to protons and hypernuclei to hyperons. The other is their
 626 centrality-dependent yield ratios.

627 Fig. 13 (a) and (b) show the $\langle p_T \rangle$ ratios of dibaryon 627 Fig. 13 (a) and (b) show the $\langle p_T \rangle$ ratios of dibaryon
 628 states to baryons and those of tribaryon states to baryons, 628 states to baryons and those of tribaryon states to baryons,
 629 i.e., $\frac{\langle p_T \rangle_d}{\langle p_T \rangle_p}$, $\frac{\langle p_T \rangle_{H(p\Omega^-)}}{\langle p_T \rangle_{\Omega^-}}$, $\frac{\langle p_T \rangle_{H(n\Omega^-)}}{\langle p_T \rangle_{\Omega^-}}$, $\frac{\langle p_T \rangle_t}{\langle p_T \rangle_p}$, $\frac{\langle p_T \rangle_{^3\text{He}}}{\langle p_T \rangle_p}$, $\frac{\langle p_T \rangle_{^3\Lambda\text{H}}}{\langle p_T \rangle_\Lambda}$ 629 i.e., $\frac{\langle p_T \rangle_d}{\langle p_T \rangle_p}$, $\frac{\langle p_T \rangle_{H(p\Omega^-)}}{\langle p_T \rangle_{\Omega^-}}$, $\frac{\langle p_T \rangle_{H(n\Omega^-)}}{\langle p_T \rangle_{\Omega^-}}$, $\frac{\langle p_T \rangle_t}{\langle p_T \rangle_p}$, $\frac{\langle p_T \rangle_{^3\text{He}}}{\langle p_T \rangle_p}$, $\frac{\langle p_T \rangle_{^3\Lambda\text{H}}}{\langle p_T \rangle_\Lambda}$
 630 and $\frac{\langle p_T \rangle_{H(pn\Omega^-)}}{\langle p_T \rangle_{\Omega^-}}$. Open symbols connected by dashed lines 630 and $\frac{\langle p_T \rangle_{H(pn\Omega^-)}}{\langle p_T \rangle_{\Omega^-}}$. Open symbols connected by dashed lines
 631 to guide the eye are the theoretical results of the coales- 631 to guide the eye are the theoretical results of the coales-

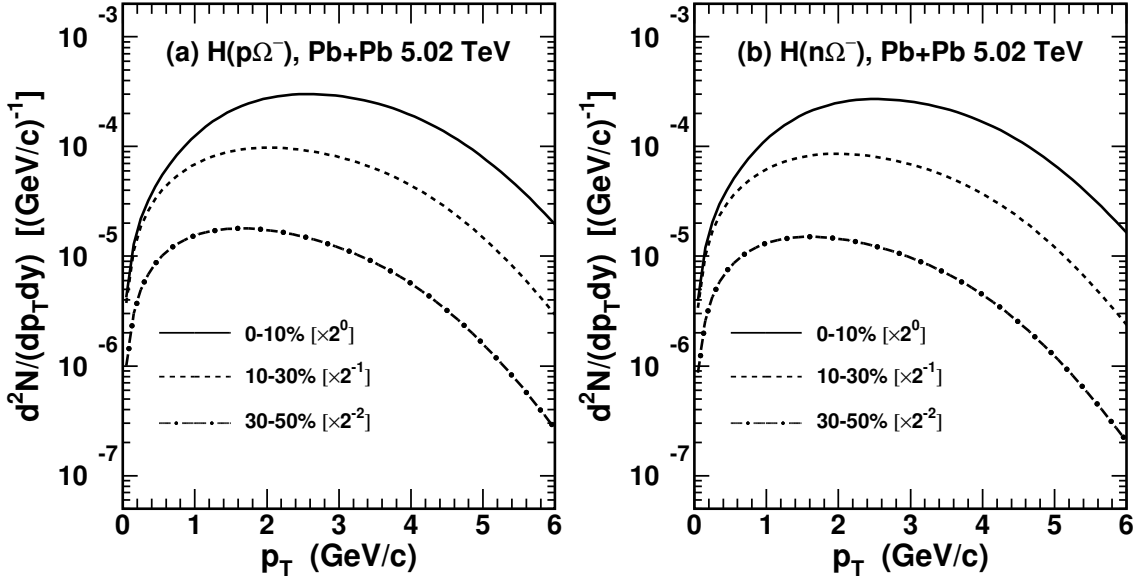


Fig. 11. Predictions of the p_T spectra of (a) $H(p\Omega^-)$ and (b) $H(n\Omega^-)$ in different centralities in Pb+Pb collisions at $\sqrt{s_{NN}} = 5.02$ TeV.

Table 4. Predictions of averaged transverse momenta $\langle p_T \rangle$ and yield rapidity densities dN/dy of $H(pn\Omega^-)$ in different centralities in Pb+Pb collisions at $\sqrt{s_{NN}} = 5.02$ TeV. Theory-1.5, Theory-2.0, and Theory-2.5 denote theoretical results at $R_{H(pn\Omega^-)} = 1.5, 2.0, 2.5$ fm, respectively.

Centrality	$\langle p_T \rangle$ (GeV/c)			dN/dy ($\times 10^{-6}$)		
	Theory-1.5	Theory-2.0	Theory-2.5	Theory-1.5	Theory-2.0	Theory-2.5
0 – 10%	3.94	3.88	3.82	4.77	4.17	3.56
$H(pn\Omega^-)$ 10 – 30%	3.44	3.36	3.29	3.50	2.95	2.41
30 – 50%	2.98	2.89	2.81	1.60	1.24	0.92

cence model. All these $\langle p_T \rangle$ ratios increase as a function of $dN_{ch}/d\eta$ due to the stronger collective flow in more central collisions. More interestingly, these $\langle p_T \rangle$ ratios of light nuclei to protons and hypernuclei to hyperons happen to offset the $\langle p_T \rangle$ differences of p , Λ and Ω^- . This makes them more powerful to bring characteristics resulting from the production mechanism to light. Both dibaryon-to-baryon and tribaryon-to-baryon $\langle p_T \rangle$ ratios exhibit a reverse hierarchy of the nucleus sizes at any centrality, i.e., $\frac{\langle p_T \rangle_d}{\langle p_T \rangle_p} > \frac{\langle p_T \rangle_{H(p\Omega^-)}}{\langle p_T \rangle_{\Omega^-}} > \frac{\langle p_T \rangle_{H(n\Omega^-)}}{\langle p_T \rangle_{\Omega^-}}$ as $R_d < R_{H(p\Omega^-)} < R_{H(n\Omega^-)}$, and $\frac{\langle p_T \rangle_t}{\langle p_T \rangle_p} > \frac{\langle p_T \rangle_{^3\text{He}}}{\langle p_T \rangle_p} > \frac{\langle p_T \rangle_{H(pn\Omega^-)}}{\langle p_T \rangle_{\Omega^-}} > \frac{\langle p_T \rangle_{^3\text{H}}}{\langle p_T \rangle_{\Lambda}}$ as $R_t < R_{^3\text{He}} < R_{H(pn\Omega^-)} < R_{^3\text{H}}$. Here we take results of $H(pn\Omega^-)$ at $R_{H(pn\Omega^-)} = 2$ fm for exhibition, and those at $R_{H(pn\Omega^-)} = 1.5, 2.5$ fm give the same conclusion, a reverse hierarchy of the nucleus size. Such reverse hierarchy comes from stronger production suppression for light (hyper-) nuclei with larger sizes in higher p_T regions. This production property is very different from the thermal model in which these ratios are approximately equal to each other [47].

Fig. 13 (c) and (d) show yield ratios of dibaryon states to baryons and those of tribaryon states to baryons. Open symbols connected with dashed lines to guide the eye are the theo-

retical results of the coalescence model. Some of these ratios such as d/p , t/p , $^3\text{He}/p$ and $H(pn\Omega^-)/\Omega^-$ decrease while the others $H(p\Omega^-)/\Omega^-$, $H(n\Omega^-)/\Omega^-$ and $^3\text{H}/\Lambda$ increase as a function of $dN_{ch}/d\eta$. From Eqs. (15) and (27), similar as Eq. (34), we approximately have

$$\begin{aligned}
 \frac{d}{p} &\sim \frac{H(p\Omega^-)}{\Omega^-} \sim \frac{H(n\Omega^-)}{\Omega^-} \\
 &\propto \frac{N_p}{\langle R_f \rangle^3 \left(C_0 + \frac{\sigma^2}{\langle R_f \rangle^2} \right) \sqrt{\frac{C_0}{\langle \gamma \rangle^2} + \frac{\sigma^2}{\langle R_f \rangle^2}}} \\
 &= \frac{N_p}{\langle R_f \rangle^3 / \langle \gamma \rangle} \times \frac{1}{\left(C_0 + \frac{\sigma^2}{\langle R_f \rangle^2} \right) \sqrt{C_0 + \frac{\sigma^2}{\langle R_f \rangle^2 / \langle \gamma \rangle^2}}}, \quad (35)
 \end{aligned}$$

and

$$\begin{aligned}
 \frac{t}{p} &\sim \frac{^3\text{He}}{p} \sim \frac{^3\text{H}}{\Lambda} \sim \frac{H(pn\Omega^-)}{\Omega^-} \\
 &\propto \frac{N_p^2}{\langle R_f \rangle^6 \left(C_0 + \frac{\sigma_1^2}{\langle R_f \rangle^2} \right) \sqrt{\frac{C_0}{\langle \gamma \rangle^2} + \frac{\sigma_1^2}{\langle R_f \rangle^2}}} \\
 &\times \frac{1}{\left(\frac{4C_0}{3} + \frac{\sigma_2^2}{\langle R_f \rangle^2} \right) \sqrt{\frac{4C_0}{3\langle \gamma \rangle^2} + \frac{\sigma_2^2}{\langle R_f \rangle^2}}}
 \end{aligned}$$

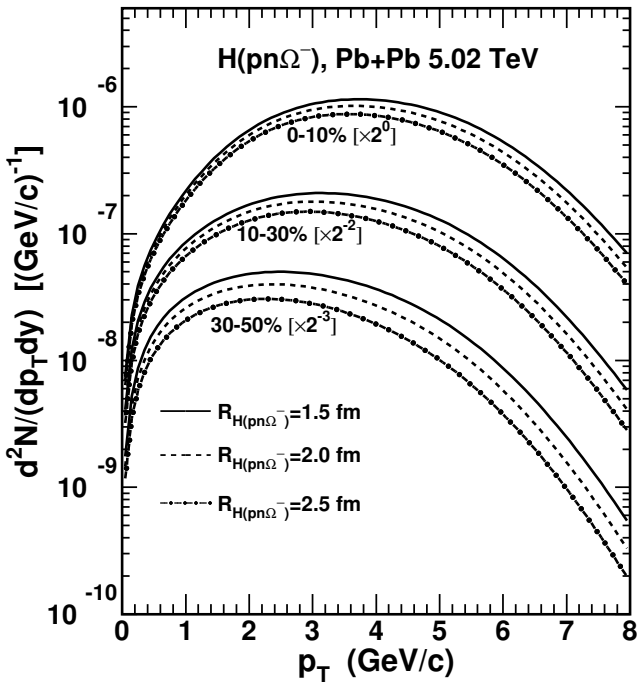


Fig. 12. Predictions of the p_T spectra of $H(pn\Omega^-)$ in different centralities in Pb+Pb collisions at $\sqrt{s_{NN}} = 5.02$ TeV.

$$666 \quad = \left(\frac{N_p}{\langle R_f \rangle^3 / \langle \gamma \rangle} \right)^2 \frac{1}{\left(C_0 + \frac{\sigma_1^2}{\langle R_f \rangle^2} \right) \sqrt{C_0 + \frac{\sigma_1^2}{\langle R_f \rangle^2 / \langle \gamma \rangle^2}}} \\ 667 \quad \times \frac{1}{\left(\frac{4C_0}{3} + \frac{\sigma_2^2}{\langle R_f \rangle^2} \right) \sqrt{\frac{4C_0}{3} + \frac{\sigma_2^2}{\langle R_f \rangle^2 / \langle \gamma \rangle^2}}}. \quad (36)$$

668 Eqs. (35) and (36) show that behaviors of these two-particle
669 yield ratios closely relate with the nucleon number density
670 $\frac{N_p}{\langle R_f \rangle^3 / \langle \gamma \rangle}$ and the production suppression effect items of the
671 relative size of nuclei to hadronic source systems $\frac{\sigma_1}{\langle R_f \rangle}$, $\frac{\sigma_1}{\langle R_f \rangle}$
672 and $\frac{\sigma_2}{\langle R_f \rangle}$.

673 For the limit case of the nuclei with very small (negligible)
674 sizes compared to the hadronic system scale, the $dN_{ch}/d\eta$ -
675 dependent behaviors of their yield ratios to baryons are com-
676 pletely determined by the nucleon number density. For the
677 general case, the item $\frac{\sigma_i}{\langle R_f \rangle}$ suppresses these ratios and such
678 suppression becomes weaker in larger hadronic systems. This
679 makes these yield ratios increase from peripheral to central
680 collisions, i.e., with the increasing $dN_{ch}/d\eta$. The larger
681 the nucleus size, the stronger the increase as a function of
682 $dN_{ch}/d\eta$. The nucleon density decreases with increasing
683 $dN_{ch}/d\eta$ [80], which makes these ratios decrease. As the

684 root-mean-square radii of d , t , ^3He and $H(pn\Omega^-)$ are about
685 or smaller than 2 fm, the decreasing nucleon density dom-
686 inates the behaviors of their yield ratios to baryons. But
687 for $H(p\Omega^-)$, $H(n\Omega^-)$ and ^3H , their root-mean-square radii
688 are larger than 3 fm, the production suppression effect from
689 their sizes becomes dominant, which leads their yield ratios
690 to baryons increase as a function of $dN_{ch}/d\eta$. Such differ-
691 ent centrality-dependent behaviors can help justify their own
692 sizes of more light nuclei and hypernuclei in future experi-
693 ments.

V. SUMMARY

694 We extended the analytical coalescence model previously
695 developed for the productions of light nuclei to include the
696 hyperon coalescence to study production characteristics of d ,
697 ^3He , t , ^3H and Ω -hypernuclei simultaneously. We derived the
698 formulae of the momentum distributions of two baryons coa-
699 lesing into dibaryon states and three baryons coalescing into
700 tribaryon states. The relationships of dibaryon states and trib-
701 aryon states with primordial baryons in momentum space in
702 the laboratory frame were given. The effects of the hadronic
703 system scale and the nucleus's own size on the nucleus pro-
704 duction were clearly presented.

705 We applied the extended coalescence model to Pb+Pb col-
706 lisions at $\sqrt{s_{NN}} = 5.02$ TeV. We explained the available
707 data of the B_2 and B_3 , the p_T spectra, averaged transverse
708 momenta and yield rapidity densities of the d , ^3He , t , and
709 ^3H measured by the ALICE collaboration. We provided
710 predictions of the p_T spectra, averaged transverse momenta,
711 and yield rapidity densities of different Ω -hypernuclei, e.g.,
712 $H(p\Omega^-)$, $H(n\Omega^-)$, and $H(pn\Omega^-)$, for future experimental
713 measurements.

714 More interestingly, we found two groups of novel observ-
715 ables. One referred to the averaged transverse momentum
716 ratio $\frac{\langle p_T \rangle_d}{\langle p_T \rangle_p}$, $\frac{\langle p_T \rangle_{H(p\Omega^-)}}{\langle p_T \rangle_{\Omega^-}}$, $\frac{\langle p_T \rangle_{H(n\Omega^-)}}{\langle p_T \rangle_{\Omega^-}}$, $\frac{\langle p_T \rangle_t}{\langle p_T \rangle_p}$, $\frac{\langle p_T \rangle_{^3\text{He}}}{\langle p_T \rangle_p}$, $\frac{\langle p_T \rangle_{^3\text{H}}}{\langle p_T \rangle_{\Lambda}}$,
717 $\frac{\langle p_T \rangle_{H(pn\Omega^-)}}{\langle p_T \rangle_{\Omega^-}}$. They exhibited a reverse hierarchy according
718 to the sizes of the nuclei themselves at any collision central-
719 ity. The other group involved the centrality-dependent yield
720 ratios $\frac{d}{p} \frac{H(p\Omega^-)}{\Omega^-}$, $\frac{H(n\Omega^-)}{\Omega^-}$, $\frac{t}{p} \frac{^3\text{He}}{\Omega^-}$, $\frac{^3\text{H}}{\Lambda}$ and $\frac{H(pn\Omega^-)}{\Omega^-}$. Some
721 of these yield ratios $\frac{d}{p}$, $\frac{t}{p}$, $\frac{^3\text{He}}{p}$ and $\frac{H(pn\Omega^-)}{\Omega^-}$ decreased while
722 the others $\frac{H(p\Omega^-)}{\Omega^-}$, $\frac{H(n\Omega^-)}{\Omega^-}$ and $\frac{^3\text{H}}{\Lambda}$ increased as a function
723 of $dN_{ch}/d\eta$. Such different trends were caused by different
724 production suppression degrees from the nucleus sizes. The
725 behaviors of these two groups of ratios in the coalescence
726 mechanism were different from the thermal model. They
727 were powerful observables for probing the production mech-
728 anism of light (hyper-)nuclei. They unfolded the production
729 relations of different sorts of nuclei in the coalescence frame.

731 [1] J. Aichelin, 'Quantum' molecular dynamics: A Dynamical mi-
732 croscopic n body approach to investigate fragment formation

733 and the nuclear equation of state in heavy ion collisions. Phys.
734 Rept. **202**, 233–360 (1991). doi:[10.1016/0370-1573\(91\)90094-4](https://doi.org/10.1016/0370-1573(91)90094-4)

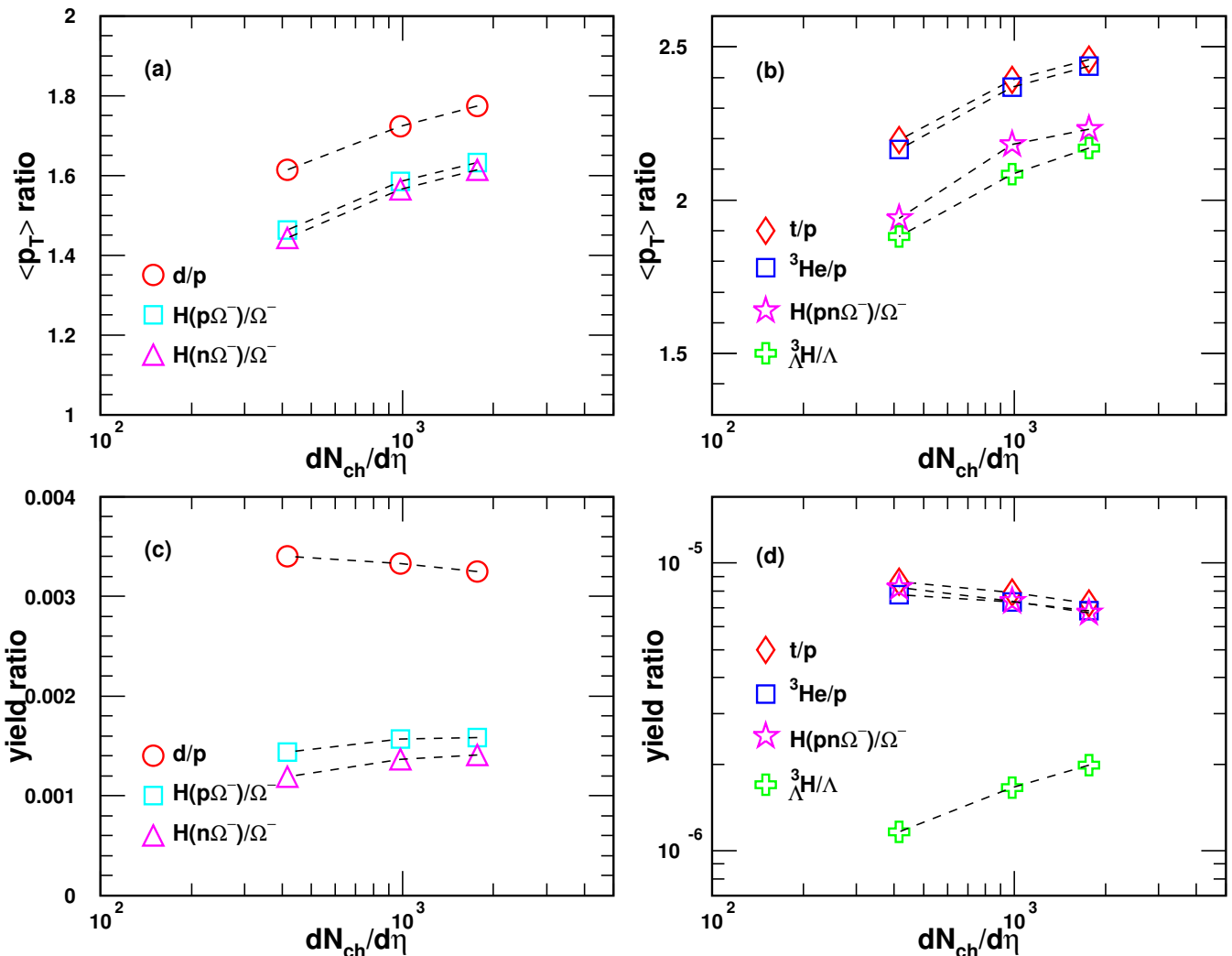


Fig. 13. The $\langle p_T \rangle$ ratios of (a) dibaryon states to baryons, (b) tribaryon states to baryons, and the yield ratios of (c) dibaryon states to baryons, (d) tribaryon states to baryons as a function of $dN_{ch}/d\eta$ in Pb+Pb collisions at $\sqrt{s_{NN}} = 5.02$ TeV. Different open symbols connected with dashed lines to guide the eye are the theoretical results.

735 3
736 [2] K.J. Sun, R. Wang, C.M. Ko et al., Unveiling the dynamics of
737 little-bang nucleosynthesis. *Nature Commun.* **15**, 1074 (2024).
738 [arXiv:2207.12532](https://arxiv.org/abs/2207.12532), doi:10.1038/s41467-024-45474-x
739 [3] A. Andronic, P. Braun-Munzinger, K. Redlich et al., Decoding
740 the phase structure of QCD via particle production at
741 high energy. *Nature* **561**, 321–330 (2018). [arXiv:1710.09425](https://arxiv.org/abs/1710.09425),
742 doi:10.1038/s41586-018-0491-6
743 [4] K.J. Sun, L.W. Chen, C.M. Ko et al., Probing QCD critical
744 fluctuations from light nuclei production in relativistic
745 heavy-ion collisions. *Phys. Lett. B* **774**, 103–107 (2017).
746 [arXiv:1702.07620](https://arxiv.org/abs/1702.07620), doi:10.1016/j.physletb.2017.09.056
747 [5] K.J. Sun, L.W. Chen, C.M. Ko et al., Light nuclei production as a probe of the QCD phase diagram.
748 *Phys. Lett. B* **781**, 499–504 (2018). [arXiv:1801.09382](https://arxiv.org/abs/1801.09382),
749 doi:10.1016/j.physletb.2018.04.035
750 [6] A. Bzdak, S. Esumi, V. Koch et al., Mapping the
751 Phases of Quantum Chromodynamics with Beam Energy
752 Scan. *Phys. Rept.* **853**, 1–87 (2020). [arXiv:1906.00936](https://arxiv.org/abs/1906.00936),
753
754 754 doi:10.1016/j.physrep.2020.01.005
755 [7] X. Luo, S. Shi, N. Xu et al., A Study of the Properties
756 of the QCD Phase Diagram in High-Energy Nuclear
757 Collisions. *Particles* **3**, 278–307 (2020). [arXiv:2004.00789](https://arxiv.org/abs/2004.00789),
758 doi:10.3390/particles3020022
759 [8] H. Liu, D. Zhang, S. He et al., Light nuclei production
760 in Au+Au collisions at $s_{NN} = 5–200$ GeV from
761 JAM model. *Phys. Lett. B* **805**, 135452 (2020). [Erratum: *Phys.Lett.B* 829, 137132 (2022)]. [arXiv:1909.09304](https://arxiv.org/abs/1909.09304),
762 doi:10.1016/j.physletb.2020.135452
763 [9] J. Steinheimer, M. Mitrovski, T. Schuster et al.,
764 Strangeness fluctuations and MEMO production at FAIR.
765 *Phys. Lett. B* **676**, 126–131 (2009). [arXiv:0811.4077](https://arxiv.org/abs/0811.4077),
766 doi:10.1016/j.physletb.2009.04.062
767 [10] T. Shao, J. Chen, C.M. Ko et al., Yield ratio of hypertriton to
768 light nuclei in heavy-ion collisions from $\sqrt{s_{NN}} = 4.9$ GeV to
769 2.76 TeV. *Chin. Phys. C* **44**, 114001 (2020). [arXiv:2004.02385](https://arxiv.org/abs/2004.02385),
770 doi:10.1088/1674-1137/abaf00
771 [11] J.L. Nagle, B.S. Kumar, M.J. Bennett et al., Source size deter-
772

mination in relativistic nucleus-nucleus collisions. Phys. Rev. Lett. **73**, 1219–1222 (1994). doi:10.1103/PhysRevLett.73.1219

[12] J. Chen, D. Keane, Y.G. Ma et al., Antinuclei in Heavy-Ion Collisions. Phys. Rept. **760**, 1–39 (2018). arXiv:1808.09619, doi:10.1016/j.physrep.2018.07.002

[13] K. Blum, M. Takimoto, Nuclear coalescence from correlation functions. Phys. Rev. C **99**, 044913 (2019). arXiv:1901.07088, doi:10.1103/PhysRevC.99.044913

[14] S. Bazak, S. Mrowczynski, Production of ^4Li and $p - ^3\text{He}$ correlation function in relativistic heavy-ion collisions. Eur. Phys. J. A **56**, 193 (2020). arXiv:2001.11351, doi:10.1140/epja/s10050-020-00198-6

[15] H.H. Gutbrod, A. Sandoval, P.J. Johansen et al., Final State Interactions in the Production of Hydrogen and Helium Isotopes by Relativistic Heavy Ions on Uranium. Phys. Rev. Lett. **37**, 667–670 (1976). doi:10.1103/PhysRevLett.37.667

[16] Y.X. Zhang, S. Zhang, Y.G. Ma, Deuteron production mechanism via azimuthal correlation for $p - p$ and $p\text{-Pb}$ collisions at LHC energy with the AMPT model. Eur. Phys. J. A **59**, 72 (2023). doi:10.1140/epja/s10050-023-00980-2

[17] S.R. Beane, E. Chang, S.D. Cohen et al., Light Nuclei and Hypernuclei from Quantum Chromodynamics in the Limit of SU(3) Flavor Symmetry. Phys. Rev. D **87**, 034506 (2013). arXiv:1206.5219, doi:10.1103/PhysRevD.87.034506

[18] H. Nemura, Y. Suzuki, Y. Fujiwara et al., Study of light Lambda and Lambda-Lambda hypernuclei with the stochastic variational method and effective Lambda N potentials. Prog. Theor. Phys. **103**, 929–958 (2000). arXiv:nucl-th/9912065, doi:10.1143/PTP.103.929

[19] Y.G. Ma, Hypernuclei as a laboratory to test hyperon-nucleon interactions. Nucl. Sci. Tech. **34**, 97 (2023). doi:10.1007/s41365-023-01248-6

[20] P. Junnarkar, N. Mathur, Deuteronlike Heavy Dibaryons from Lattice Quantum Chromodynamics. Phys. Rev. Lett. **123**, 162003 (2019). arXiv:1906.06054, doi:10.1103/PhysRevLett.123.162003

[21] K. Morita, S. Gongyo, T. Hatsuda et al., Probing $\Omega\Omega$ and $p\Omega$ dibaryons with femtoscopic correlations in relativistic heavy-ion collisions. Phys. Rev. C **101**, 015201 (2020). arXiv:1908.05414, doi:10.1103/PhysRevC.101.015201

[22] S. Afanasiev et al., Elliptic flow for phi mesons and (anti)deuterons in Au + Au collisions at $s(\text{NN})^{**}(1/2) = 200\text{-GeV}$. Phys. Rev. Lett. **99**, 052301 (2007). arXiv:nucl-ex/0703024, doi:10.1103/PhysRevLett.99.052301

[23] T. Anticic et al., Production of deuterium, tritium, and He3 in central Pb + Pb collisions at 20A,30A,40A,80A, and 158A GeV at the CERN Super Proton Synchrotron. Phys. Rev. C **94**, 044906 (2016). arXiv:1606.04234, doi:10.1103/PhysRevC.94.044906

[24] C. Adler et al., Anti-deuteron and anti-He-3 production in $s(\text{NN})^{**}(1/2) = 130\text{-GeV}$ Au+Au collisions. Phys. Rev. Lett. **87**, 262301 (2001). [Erratum: Phys. Rev. Lett. 87, 279902 (2001)]. arXiv:nucl-ex/0108022, doi:10.1103/PhysRevLett.87.262301

[25] L. Adamczyk et al., Measurement of elliptic flow of light nuclei at $\sqrt{s_{\text{NN}}} = 200, 62.4, 39, 27, 19.6, 11.5$, and 7.7 GeV at the BNL Relativistic Heavy Ion Collider. Phys. Rev. C **94**, 034908 (2016). arXiv:1601.07052, doi:10.1103/PhysRevC.94.034908

[26] J. Adam et al., Beam-energy dependence of the directed flow of deuterons in Au+Au collisions. Phys. Rev. C **102**, 044906 (2020). arXiv:2007.04609, doi:10.1103/PhysRevC.102.044906

[27] J. Adam et al., Beam energy dependence of (anti-)deuteron production in Au + Au collisions at the BNL Relativistic Heavy Ion Collider. Phys. Rev. C **99**, 064905 (2019). arXiv:1903.11778, doi:10.1103/PhysRevC.99.064905

[28] M. Abdulhamid et al., Beam Energy Dependence of Triton Production and Yield Ratio ($N_t \times N_p / N_d^2$) in Au+Au Collisions at RHIC. Phys. Rev. Lett. **130**, 202301 (2023). arXiv:2209.08058, doi:10.1103/PhysRevLett.130.202301

[29] S. Acharya et al., Elliptic and triangular flow of (anti)deuterons in Pb-Pb collisions at $\sqrt{s_{\text{NN}}} = 5.02\text{ TeV}$. Phys. Rev. C **102**, 055203 (2020). arXiv:2005.14639, doi:10.1103/PhysRevC.102.055203

[30] S. Acharya et al., Light (anti)nuclei production in Pb-Pb collisions at $s_{\text{NN}}=5.02\text{ TeV}$. Phys. Rev. C **107**, 064904 (2023). arXiv:2211.14015, doi:10.1103/PhysRevC.107.064904

[31] J. Adam et al., Measurement of the mass difference and the binding energy of the hypertriton and antihypertriton. Nature Phys. **16**, 409–412 (2020). arXiv:1904.10520, doi:10.1038/s41567-020-0799-7

[32] M. Abdallah et al., Measurements of H_Λ^3 and H_Λ^4 Lifetimes and Yields in Au+Au Collisions in the High Baryon Density Region. Phys. Rev. Lett. **128**, 202301 (2022). arXiv:2110.09513, doi:10.1103/PhysRevLett.128.202301

[33] S. Acharya et al., Measurement of the Lifetime and Λ Separation Energy of $\Lambda\bar{\Lambda}3$. Phys. Rev. Lett. **131**, 102302 (2023). arXiv:2209.07360, doi:10.1103/PhysRevLett.131.102302

[34] J. Adam et al., ^3H and $^3\bar{\Lambda}\bar{\Lambda}$ production in Pb-Pb collisions at $\sqrt{s_{\text{NN}}} = 2.76\text{ TeV}$. Phys. Lett. B **754**, 360–372 (2016). arXiv:1506.08453, doi:10.1016/j.physletb.2016.01.040

[35] J. Chen et al., Properties of the QCD matter: review of selected results from the relativistic heavy ion collider beam energy scan (RHIC BES) program. Nucl. Sci. Tech. **35**, 214 (2024). arXiv:2407.02935, doi:10.1007/s41365-024-01591-2

[36] P. Braun-Munzinger, B. Dönigus, Loosely-bound objects produced in nuclear collisions at the LHC. Nucl. Phys. A **987**, 144–201 (2019). arXiv:1809.04681, doi:10.1016/j.nuclphysa.2019.02.006

[37] D. Oliinchenko, Overview of light nuclei production in relativistic heavy-ion collisions. Nucl. Phys. A **1005**, 121754 (2021). arXiv:2003.05476, doi:10.1016/j.nuclphysa.2020.121754

[38] S. Mrowczynski, Production of light nuclei at colliders – coalescence vs. thermal model. Eur. Phys. J. ST **229**, 3559–3583 (2020). arXiv:2004.07029, doi:10.1140/epjst/e2020-000067-0

[39] B. Dönigus, G. Röpke, D. Blaschke, Deuteron yields from heavy-ion collisions at energies available at the CERN Large Hadron Collider: Continuum correlations and in-medium effects. Phys. Rev. C **106**, 044908 (2022). arXiv:2206.10376, doi:10.1103/PhysRevC.106.044908

[40] C.B. Dover, U.W. Heinz, E. Schnedermann et al., Relativistic coalescence model for high-energy nuclear collisions. Phys. Rev. C **44**, 1636–1654 (1991). doi:10.1103/PhysRevC.44.1636

[41] L.W. Chen, C.M. Ko, B.A. Li, Light clusters production as a probe to the nuclear symmetry energy. Phys. Rev. C **68**, 017601 (2003). arXiv:nucl-th/0302068, doi:10.1103/PhysRevC.68.017601

[42] P. Liu, J.H. Chen, Y.G. Ma et al., Production of light nuclei and hypernuclei at High Intensity Accelerator Facility energy region. Nucl. Sci. Tech. **28**, 55 (2017). [Erratum: Nucl. Sci. Tech. 28, 89 (2017)]. doi:10.1007/s41365-017-0207-x

[43] L.L. Zhu, B. Wang, M. Wang et al., Energy and centrality dependence of light nuclei production in relativistic heavy-ion collisions. Nucl. Sci. Tech. **33**, 45 (2022). doi:10.1007/s41365-022-01028-8

899 [44] K.J. Sun, C.M. Ko, Event-by-event antideuteron multi- 962
900 plicity fluctuation in Pb+Pb collisions at $s_{NN}=5.02$ TeV. 963
901 Phys. Lett. B **840**, 137864 (2023). [arXiv:2204.10879](https://arxiv.org/abs/2204.10879), 964
902 doi:10.1016/j.physletb.2023.137864 965

903 [45] R. Wang, Y.G. Ma, L.W. Chen et al., Kinetic approach of 966
904 light-nuclei production in intermediate-energy heavy-ion col- 967
905 lisions. Phys. Rev. C **108**, L031601 (2023). [arXiv:2305.02988](https://arxiv.org/abs/2305.02988), 968
906 doi:10.1103/PhysRevC.108.L031601 969

907 [46] F. Li, S. Zhang, K.J. Sun et al., Production of light 970
908 nuclei in isobaric Ru + Ru and Zr + Zr collisions at 971
909 $s_{NN}=7.7-200$ GeV from a multiphase transport model. 972
910 Phys. Rev. C **109**, 064912 (2024). [arXiv:2405.11558](https://arxiv.org/abs/2405.11558), 973
911 doi:10.1103/PhysRevC.109.064912 974

912 [47] A. Andronic, P. Braun-Munzinger, J. Stachel et al., Produc- 975
913 tion of light nuclei, hypernuclei and their antiparticles in rela- 976
914 tivistic nuclear collisions. Phys. Lett. B **697**, 203–207 (2011). 977
915 [arXiv:1010.2995](https://arxiv.org/abs/1010.2995), doi:10.1016/j.physletb.2011.01.053 978

916 [48] A. Mekjian, Thermodynamic Model for Composite Particle 979
917 Emission in Relativistic Heavy Ion Collisions. Phys. Rev. Lett. 980
918 **38**, 640–643 (1977). doi:10.1103/PhysRevLett.38.640 981

919 [49] P.J. Siemens, J.I. Kapusta, EVIDENCE FOR A SOFT NU- 982
920 CLEAR MATTER EQUATION OF STATE. Phys. Rev. Lett. 983
921 **43**, 1486–1489 (1979). doi:10.1103/PhysRevLett.43.1486 984

922 [50] J. Cleymans, S. Kabana, I. Kraus et al., Antimatter produc- 985
923 tion in proton-proton and heavy-ion collisions at ultrarelativistic 986
924 energies. Phys. Rev. C **84**, 054916 (2011). [arXiv:1105.3719](https://arxiv.org/abs/1105.3719), 987
925 doi:10.1103/PhysRevC.84.054916 988

926 [51] Y. Cai, T.D. Cohen, B.A. Gelman et al., Yields of weakly- 989
927 bound light nuclei as a probe of the statistical hadronization 990
928 model. Phys. Rev. C **100**, 024911 (2019). [arXiv:1905.02753](https://arxiv.org/abs/1905.02753), 991
929 doi:10.1103/PhysRevC.100.024911 992

930 [52] A. Schwarzschild, C. Zupancic, Production of Tritons, 993
931 Deuterons, Nucleons, and Mesons by 30-GeV Protons on 994
932 A-1, Be, and Fe Targets. Phys. Rev. **129**, 854–862 (1963). 995
933 doi:10.1103/PhysRev.129.854 996

934 [53] H. Sato, K. Yazaki, On the coalescence model for high- 997
935 energy nuclear reactions. Phys. Lett. B **98**, 153–157 (1981). 998
936 doi:10.1016/0370-2693(81)90976-X 999

937 [54] R. Mattiello, A. Jahns, H. Sorge et al., Deuteron flow in ultra- 1000
938 relativistic heavy ion reactions. Phys. Rev. Lett. **74**, 2180–2183 1001
939 (1995). doi:10.1103/PhysRevLett.74.2180 1002

940 [55] J.L. Nagle, B.S. Kumar, D. Kusnezov et al., Coalescence of 1003
941 deuterons in relativistic heavy ion collisions. Phys. Rev. C **53**, 1004
942 367–376 (1996). doi:10.1103/PhysRevC.53.367 1005

943 [56] R. Mattiello, H. Sorge, H. Stocker et al., Nuclear clusters as a 1006
944 probe for expansion flow in heavy ion reactions at 10-A/GeV 1007
945 - 15-A/GeV. Phys. Rev. C **55**, 1443–1454 (1997). [arXiv:nucl- 1008
946 th/9607003](https://arxiv.org/abs/nucl-th/9607003), doi:10.1103/PhysRevC.55.1443 1009

947 [57] A. Polleri, J.P. Bondorf, I.N. Mishustin, Effects of collective 1010
948 expansion on light cluster spectra in relativistic heavy ion colli- 1011
949 sions. Phys. Lett. B **419**, 19–24 (1998). [arXiv:nucl-th/9711011](https://arxiv.org/abs/nucl-th/9711011), 1012
950 doi:10.1016/S0370-2693(97)01455-X 1013

951 [58] N. Sharma, T. Perez, A. Castro et al., Methods for separation 1014
952 of deuterons produced in the medium and in jets in high energy 1015
953 collisions. Phys. Rev. C **98**, 014914 (2018). [arXiv:1803.02313](https://arxiv.org/abs/1803.02313), 1016
954 doi:10.1103/PhysRevC.98.014914 1017

955 [59] R. Scheibl, U.W. Heinz, Coalescence and flow in ultrarelativis- 1018
956 tic heavy ion collisions. Phys. Rev. C **59**, 1585–1602 (1999). 1019
957 [arXiv:nucl-th/9809092](https://arxiv.org/abs/nucl-th/9809092), doi:10.1103/PhysRevC.59.1585 1020

958 [60] W. Zhao, L. Zhu, H. Zheng et al., Spectra and flow of light 1021
959 nuclei in relativistic heavy ion collisions at energies avail- 1022
960 able at the BNL Relativistic Heavy Ion Collider and at the 1023
961 CERN Large Hadron Collider. Phys. Rev. C **98**, 054905 (2018). 1024

61 [61] Y.H. Feng, C.M. Ko, Y.G. Ma et al., Jet-induced enhance- 963
964 ment of deuteron production in pp and p-Pb collisions at the 965
966 LHC. Phys. Lett. B **859**, 139102 (2024). [arXiv:2408.01634](https://arxiv.org/abs/2408.01634), 967
968 doi:10.1016/j.physletb.2024.139102 969

62 [62] T.T. Wang, Y.G. Ma, Nucleon-number scalings of anisotropic 970
967 flows and nuclear modification factor for light nuclei in 971
968 the squeeze-out region. Eur. Phys. J. A **55**, 102 (2019). 972
969 [arXiv:2002.06067](https://arxiv.org/abs/2002.06067), doi:10.1140/epja/i2019-12788-0 973

63 [63] W. Zhao, K.J. Sun, C.M. Ko et al., Multiplicity scaling 974
971 of light nuclei production in relativistic heavy-ion colli- 972
973 sions. Phys. Lett. B **820**, 136571 (2021). [arXiv:2105.14204](https://arxiv.org/abs/2105.14204), 974
975 doi:10.1016/j.physletb.2021.136571 976

64 [64] X.Y. Zhao, Y.T. Feng, F.L. Shao et al., Production char- 977
976 acteristics of light (anti-)nuclei from (anti-)nucleon coales- 977
977 cence in heavy ion collisions at energies employed at the 978
978 RHIC beam energy scan. Phys. Rev. C **105**, 054908 (2022). 979
979 [arXiv:2201.10354](https://arxiv.org/abs/2201.10354), doi:10.1103/PhysRevC.105.054908 980

65 [65] R.Q. Wang, J.P. Lv, Y.H. Li et al., Different coalescence 981
980 sources of light nucleus production in Au-Au collisions at 981
982 GeV*. Chin. Phys. C **48**, 053112 (2024). [arXiv:2210.10271](https://arxiv.org/abs/2210.10271), 983
983 doi:10.1088/1674-1137/ad2b56 984

66 [66] R.Q. Wang, F.L. Shao, J. Song, Momentum dependence of 985
985 light nuclei production in $p - p$, $p - Pb$, and Pb-Pb col- 986
986 lisions at energies available at the CERN Large Hadron Col- 987
987 linder. Phys. Rev. C **103**, 064908 (2021). [arXiv:2007.05745](https://arxiv.org/abs/2007.05745), 988
988 doi:10.1103/PhysRevC.103.064908 989

67 [67] R.Q. Wang, Y.H. Li, J. Song et al., Production properties 990
990 of deuterons, tritons, and He3 via an analytical nucleon 991
991 coalescence method in Pb-Pb collisions at $s_{NN}=2.76$ TeV. 992
992 Phys. Rev. C **109**, 034907 (2024). [arXiv:2309.16296](https://arxiv.org/abs/2309.16296), 993
993 doi:10.1103/PhysRevC.109.034907 994

68 [68] S. Acharya et al., Measurement of 3 H production in Pb-Pb col- 995
994 lisions at $\sqrt{s_{NN}} = 5.02$ TeV. [arXiv:2405.19839](https://arxiv.org/abs/2405.19839) 995

69 [69] L.W. Chen, C.M. Ko, B.A. Li, Light cluster production in 996
996 intermediate-energy heavy ion collisions induced by neutron 997
997 rich nuclei. Nucl. Phys. A **729**, 809–834 (2003). [arXiv:nucl- 998
998 th/0306032](https://arxiv.org/abs/nucl-th/0306032), doi:10.1016/j.nuclphysa.2003.09.010 999

70 [70] C.M. Ko, T. Song, F. Li et al., Partonic mean-field ef- 1000
999 fects on matter and antimatter elliptic flows. Nucl. 1001
999 Phys. A **928**, 234–246 (2014). [arXiv:1211.5511](https://arxiv.org/abs/1211.5511), 1002
999 doi:10.1016/j.nuclphysa.2014.05.016 1003

71 [71] L. Zhu, C.M. Ko, X. Yin, Light (anti-)nuclei produc- 1004
999 tion and flow in relativistic heavy-ion collisions. 1005
999 Phys. Rev. C **92**, 064911 (2015). [arXiv:1510.03568](https://arxiv.org/abs/1510.03568), 1006
999 doi:10.1103/PhysRevC.92.064911 1007

72 [72] S. Mrowczynski, Production of light nuclei in the thermal 1008
999 and coalescence models. Acta Phys. Polon. B **48**, 707 (2017). 1009
999 [arXiv:1607.02267](https://arxiv.org/abs/1607.02267), doi:10.5506/APhysPolB.48.707 1010

73 [73] A. Kisiel, M. Gałażyn, P. Bożek, Pion, kaon, and proton 1011
999 femtoscopy in Pb-Pb collisions at $\sqrt{s_{NN}}=2.76$ TeV modeled 1012
999 in (3+1)D hydrodynamics. Phys. Rev. C **90**, 064914 (2014). 1013
999 [arXiv:1409.4571](https://arxiv.org/abs/1409.4571), doi:10.1103/PhysRevC.90.064914 1014

74 [74] J. Adam et al., Centrality dependence of pion freeze- 1015
999 out radii in Pb-Pb collisions at $\sqrt{s_{NN}} = 2.76$ TeV. 1016
999 Phys. Rev. C **93**, 024905 (2016). [arXiv:1507.06842](https://arxiv.org/abs/1507.06842), 1017
999 doi:10.1103/PhysRevC.93.024905 1018

75 [75] Y.L. Cheng, S. Zhang, Y.G. Ma, Collision centrality and 1019
999 system size dependences of light nuclei production via dynami- 1020
999 cal coalescence mechanism. Eur. Phys. J. A **57**, 330 (2021). 1021
999 [arXiv:2112.03520](https://arxiv.org/abs/2112.03520), doi:10.1140/epja/s10050-021-00639-w 1022

76 [76] I. Angeli, K.P. Marinova, Table of experimental nuclear ground 1023
999 state charge radii: An update. Atom. Data Nucl. Data Tabl. **99**, 1024

1025 69–95 (2013). [doi:10.1016/j.adt.2011.12.006](https://doi.org/10.1016/j.adt.2011.12.006) 1056
 1026 [77] M. Puccio, CERN-THESIS-2017-338. Ph.D. thesis, Turin U. 1057
 1027 (2017) 1058
 1028 [78] P. Chakraborty, A.K. Pandey, S. Dash, Identical-particle (pion 1059 and kaon) femtoscopy in Pb–Pb collisions at $\sqrt{s_{NN}} = 5.02$ 1060
 1029 TeV with Therminator 2 modeled with (3+1)D viscous hydro- 1061
 1030 dynamics. *Eur. Phys. J. A* **57**, 338 (2021). [arXiv:2010.12161](https://arxiv.org/abs/2010.12161), 1062
 1031 [doi:10.1140/epja/s10050-021-00647-w](https://doi.org/10.1140/epja/s10050-021-00647-w) 1063
 1032 [79] J. Adams et al., Pion interferometry in Au+Au collisions at 1064
 1033 $S_{NN}^{**}(1/2) = 200$ -GeV. *Phys. Rev. C* **71**, 044906 (2005). 1065
 1034 [arXiv:nucl-ex/0411036](https://arxiv.org/abs/nucl-ex/0411036), [doi:10.1103/PhysRevC.71.044906](https://doi.org/10.1103/PhysRevC.71.044906) 1066
 1035 [80] S. Acharya et al., Production of charged pions, kaons, 1067
 1036 and (anti-)protons in Pb–Pb and inelastic pp collisions at 1068
 1037 $\sqrt{s_{NN}} = 5.02$ TeV. *Phys. Rev. C* **101**, 044907 (2020). 1069
 1038 [arXiv:1910.07678](https://arxiv.org/abs/1910.07678), [doi:10.1103/PhysRevC.101.044907](https://doi.org/10.1103/PhysRevC.101.044907) 1070
 1039 [81] E. Schnedermann, J. Sollfrank, U.W. Heinz, Thermal phe- 1071
 1040 nomenology of hadrons from 200-A/GeV S+S collisions. 1072
 1041 *Phys. Rev. C* **48**, 2462–2475 (1993). [arXiv:nucl-th/9307020](https://arxiv.org/abs/nucl-th/9307020), 1073
 1042 [doi:10.1103/PhysRevC.48.2462](https://doi.org/10.1103/PhysRevC.48.2462) 1074
 1043 [82] J. Adam et al., Production of light nuclei and anti-nuclei in 1075
 1044 pp and Pb–Pb collisions at energies available at the CERN 1076
 1045 Large Hadron Collider. *Phys. Rev. C* **93**, 024917 (2016). 1077
 1046 [arXiv:1506.08951](https://arxiv.org/abs/1506.08951), [doi:10.1103/PhysRevC.93.024917](https://doi.org/10.1103/PhysRevC.93.024917) 1078
 1047 [83] K.J. Sun, C.M. Ko, B. Dönigus, Suppression of light 1079
 1048 nuclei production in collisions of small systems at the 1080
 1049 Large Hadron Collider. *Phys. Lett. B* **792**, 132–137 (2019). 1081
 1050 [arXiv:1812.05175](https://arxiv.org/abs/1812.05175), [doi:10.1016/j.physletb.2019.03.033](https://doi.org/10.1016/j.physletb.2019.03.033) 1082
 1051 [84] P. Kalinak, Strangeness production in Pb–Pb collisions with 1083
 1052 ALICE at the LHC. *PoS EPS-HEP* **2017**, 168 (2017). 1084
 1053 [doi:10.22323/1.314.0168](https://doi.org/10.22323/1.314.0168) 1085
 1054 [85] W.b. Chang, R.q. Wang, J. Song et al., Production of 1086
 1055 1087
 1056 Strange and Charm Hadrons in Pb+Pb Collisions at $s_{NN} =$
 1057 5.02 TeV †. *Symmetry* **15**, 400 (2023). [arXiv:2302.07546](https://arxiv.org/abs/2302.07546),
 1058 [doi:10.3390/sym15020400](https://doi.org/10.3390/sym15020400)
 1059 [86] C.A. Bertulani, Probing the size and binding en- 1060
 1061 ergy of the hypertriton in heavy ion collisions. *Phys. Lett. B* **837**, 137639 (2023). [arXiv:2211.12643](https://arxiv.org/abs/2211.12643),
 1062 [doi:10.1016/j.physletb.2022.137639](https://doi.org/10.1016/j.physletb.2022.137639)
 1063 [87] D.N. Liu, C.M. Ko, Y.G. Ma et al., Softening of the hy- 1064
 1064 pertriton transverse momentum spectrum in heavy-ion colli- 1065
 1065 sions. *Phys. Lett. B* **855**, 138855 (2024). [arXiv:2404.02701](https://arxiv.org/abs/2404.02701),
 1066 [doi:10.1016/j.physletb.2024.138855](https://doi.org/10.1016/j.physletb.2024.138855)
 1067 [88] H. Clement, On the History of Dibaryons and their Fi- 1068
 1068 nal Observation. *Prog. Part. Nucl. Phys.* **93**, 195 (2017). 1069
 1069 [arXiv:1610.05591](https://arxiv.org/abs/1610.05591), [doi:10.1016/j.ppnp.2016.12.004](https://doi.org/10.1016/j.ppnp.2016.12.004)
 1070 [89] J. Pu, K.J. Sun, C.W. Ma et al., Probing the internal struc- 1071
 1071 tures of $p\Omega$ and $\Omega\Omega$ with their production at the Large Hadron 1072
 1072 Collider. *Phys. Rev. C* **110**, 024908 (2024). [arXiv:2402.04185](https://arxiv.org/abs/2402.04185),
 1073 [doi:10.1103/PhysRevC.110.024908](https://doi.org/10.1103/PhysRevC.110.024908)
 1074 [90] T. Iritani et al., $N\Omega$ dibaryon from lattice QCD near 1075
 1075 the physical point. *Phys. Lett. B* **792**, 284–289 (2019). 1076
 1076 [arXiv:1810.03416](https://arxiv.org/abs/1810.03416), [doi:10.1016/j.physletb.2019.03.050](https://doi.org/10.1016/j.physletb.2019.03.050)
 1077 [91] H. Garcilazo, A. Valcarce, ΩNN and $\Omega\Omega N$ states. 1078
 1078 *Phys. Rev. C* **99**, 014001 (2019). [arXiv:1901.05678](https://arxiv.org/abs/1901.05678),
 1079 [doi:10.1103/PhysRevC.99.014001](https://doi.org/10.1103/PhysRevC.99.014001)
 1080 [92] S. Zhang, Y.G. Ma, Ω -dibaryon production with hadron 1081
 1081 interaction potential from the lattice QCD in relativistic 1082
 1082 heavy-ion collisions. *Phys. Lett. B* **811**, 135867 (2020). 1083
 1083 [arXiv:2007.11170](https://arxiv.org/abs/2007.11170), [doi:10.1016/j.physletb.2020.135867](https://doi.org/10.1016/j.physletb.2020.135867)
 1084 [93] L. Zhang, S. Zhang, Y.G. Ma, Production of ΩNN and $\Omega\Omega N$ 1085
 1085 in ultra-relativistic heavy-ion collisions. *Eur. Phys. J. C* **82**, 1086
 1086 416 (2022). [arXiv:2112.02766](https://arxiv.org/abs/2112.02766), [doi:10.1140/epjc/s10052-022-10336-7](https://doi.org/10.1140/epjc/s10052-022-10336-7)
 1087